PAPER • **OPEN ACCESS**

Dual-photopeak joint image reconstruction for pinhole SPECT, PET and PET-SPECT

To cite this article: Satyajit Ghosh *et al* 2026 *Phys. Med. Biol.* **71** 015017

IOP Publishing Phys. Med. Biol. 71 (2026) 015017 https://doi.org/10.1088/1361-6560/ae2ce0

Physics in Medicine & Biology

IPEM Institute of Physics and Engineering in Medicine

PAPER

Dual-photopeak joint image reconstruction for pinhole SPECT, PET and PET-SPECT

Satyajit Ghosh[1], Valerio Cosmi[1], Ruud M Ramakers[1,2], Freek J Beekman[1,3] and Marlies C Goorden[1,*]

[1] Department of Radiation Science and Technology, Delft University of Technology, Delft, The Netherlands
[2] MILabs B.V., Heidelberglaan 100, 3584 CX Utrecht, The Netherlands
[3] Free Bee International, Gouda, The Netherlands
[*] Author to whom any correspondence should be addressed.

E-mail: m.c.goorden@tudelft.nl

Keywords: actinium-225, zirconium-89, targeted alpha therapy, dual-photopeak imaging, joint reconstruction, low-count imaging, preclinical PET-SPECT

Supplementary material for this article is available online

OPEN ACCESS

RECEIVED
23 July 2025

REVISED
5 December 2025

ACCEPTED FOR PUBLICATION
15 December 2025

PUBLISHED
30 December 2025

Abstract

Objective. Many SPECT and PET radionuclides, along with radionuclides used in targeted alpha or beta therapy and their imaging surrogates have multiple gamma and/or positron emissions. Images of these radionuclides are usually obtained from the photopeak with the most convenient energy and/or highest intensity or by adding counts from different photopeaks. Smart utilization of multiple energy peaks may improve reconstructed images, especially in low-count scans. *Approach.* We investigate and compare various dual-photopeak joint reconstruction (JR) approaches, namely (i) Single-Band (SB-JR)—projections from two energy windows are summed and reconstructed with a system matrix at a single average energy, (ii) mixed Multi-Band (mMB-JR)—like SB-JR but the system matrix incorporates the element-wise contributions from the photopeak energies, (iii) Multi-Band (MB-JR)—separate projections for each window and separate system matrices at relevant gamma energies are utilized. We evaluate these methods for a multi-pinhole PET-SPECT system (VECTor, MILabs, the Netherlands) using Monte Carlo generated Derenzo phantom projections of ^{225}Ac (218 keV and 440 keV gammas), ^{226}Ac (158 keV and 230 keV gammas) and ^{89}Zr (511 keV annihilation gammas and 909 keV prompt gammas) at three different activity concentrations. A contrast-to-noise ratio (CNR) based quantitative performance analysis was done. *Main results.* The MB-JR scheme of JR showed superior visual image quality and highest CNRs in almost all cases, across all radionuclides and activity concentrations. The CNR improvement over images acquired from the single best-performing photopeak ranged from 30%–65% for ^{225}Ac, 20%–54% for ^{226}Ac, and 25%–47% for ^{89}Zr, respectively, for the smallest visible rods in the Derenzo phantom. CNR improvements/degradations for the other two methods, mMB-JR and SB-JR, were: for ^{225}Ac, −16%–51% and −21%–51%; for ^{226}Ac, 9%–61% and 0.2%–38%; and for ^{89}Zr, 19%–52% and −3%–16%, respectively. *Significance.* We believe the proposed image reconstruction methods can enhance SPECT, PET, and PET-SPECT imaging of a wide range of radionuclides that emit gamma's with multiple energies.

1. Introduction

Many SPECT and PET radionuclides (e.g. ^{111}In, ^{67}Ga, ^{201}Tl, ^{89}Zr, ^{124}I), including radionuclides for targeted alpha therapy (TAT) and targeted beta therapy (TBT) (e.g. TAT: ^{225}Ac, ^{149}Tb, ^{223}Ra, ^{211}At; TBT: ^{177}Lu, ^{131}I, ^{161}Tb) and their imaging surrogates (e.g. TAT surrogates: ^{226}Ac, ^{155}Tb, ^{131}Ba, ^{209}At; TBT surrogates: ^{111}In, ^{124}I, ^{155}Tb) have multiple gamma and/or positron emissions that can be used for imaging (details provided in table 1). In most clinical and preclinical studies, either a single gamma emission—typically the one with the most convenient energy and/or highest intensity—is utilized for imaging, or

Table 1. Examples of radionuclides with multiple photopeaks that are of interest for (bio)medical applications. Half-lives, imageable emissions with corresponding energies and intensities, and applications are given for SPECT and PET radionuclides including TAT and TBT radionuclides (with their imaging surrogates), for which joint reconstruction can be used. All positrons yield 511 keV photons for imaging. Only >5% relative intensity emissions are presented.

Radionuclide	Half-life	Imageable emissions with energy in keV (%intensity)	Application
^{111}In#	2.8 d	X-rays: 23 + 26 (82%); γ: 171 (91%), 245 (94%)	Pretherapeutic dosimetry (Wong *et al* 2010), surrogate of ^{177}Lu (Nelson *et al* 2023)
^{89}Zr†	3.3 d	X-rays: 14 (42%); γ: 511 (45%), 909 (99%)	immunoPET (Pandya *et al* 2019)
^{124}I†	4.2 d	X-rays: 27 + 31 (54%); γ: 511 (45%), 603 (63%), 723 (10%), 1691 (11%)	thyroid cancer (Jentzen *et al* 2008)
^{223}Ra‡	11.4 d	X-rays: 81 + 84 (40%); γ: 154 (6%), 269 (14%)	prostate cancer (Jarvis *et al* 2021)
^{225}Ac‡	10.0 d	γ: 218* (11%), 440* (26%)	prostate (Bidkar *et al* 2024), breast cancer (Cheal *et al* 2020)
^{211}At‡	7.2 h	X-rays: 73* + 75* (57%), 77 + 79 (19%), 85* (8%); γ: 570* (98%), 1063* (75%), 1770* (7%)	ovarian cancer (Dekempeneer *et al* 2019)
^{149}Tb‡	4.1 h	X-rays: 43 + 49 (58%), 41* + 47* (100%); γ: 150* (48%), 165 (22%), 299* (28%), 346* (24%), 352 (25%), 389 (16%), 465 (5%), 511 (12%), 652 (14%), 789* (7%), 817 (10%), 853 (13%)	pancreatic cancer (Mapanao *et al* 2025)
^{161}Tb§	6.9 d	X-rays: 45 (17%); γ: 26 (23%), 49 (17%), 75 (10%)	prostate cancer (Tschan *et al* 2023), neuroendocrine tumor (Borgna *et al* 2022)
^{177}Lu§	6.6 d	γ: 113 (6%), 208 (11%)	prostate cancer (Foxton *et al* 2025), neuroendocrine tumor (Strosberg *et al* 2017)
^{131}Ba¶	11.5 d	X-rays: 31 + 35 (96%); γ: 124 (30%), 216 (20%), 373 (14%), 496 (48%)	surrogate of ^{223}Ra (Nelson *et al* 2023)
^{226}Ac¶	1.2 d	γ: 158 (15%), 230 (22%)	surrogate of ^{225}Ac (Nelson *et al* 2023)
^{209}At¶	5.4 h	X-rays: 77 + 79 (96%), 90 + 92 (19%); γ: 195 (24%), 239 (13%), 545 (91%), 781 + 790 (147%)	surrogate of ^{211}At (Nelson *et al* 2023)
^{155}Tb¶	5.3 d	X-rays: 43 + 49 (106%); γ: 87 (32%), 105 (25%)	surrogate of ^{149}Tb and ^{161}Tb (Tagawa *et al* 2013, Nelson *et al* 2023)

Symbols: # SPECT radionuclide; † PET radionuclides; ‡ TAT radionuclides; § TBT radionuclides; ¶imaging surrogates; * emission from daughters with intensity disregarding branching ratio.

peaks are added up and reconstructed with a single system matrix (Dey *et al* 2014, Rowe *et al* 2015, Liu *et al* 2019, Ravizzini *et al* 2023). Leveraging all available gamma emissions jointly in an optimal way for imaging has the potential to further enhance imaging performance, especially in low-uptake and/or shorter time scans. A better reconstruction method may also enable to scan with a lower dose. Furthermore, the development of specialized low-count imaging methods is essential to facilitate image-based dosimetry for TAT radionuclides, given the often low gamma-abundancies and/or limitations on the maximum injectable activity permissible (Nedrow *et al* 2017, Cheal *et al* 2020, Kelly *et al* 2020, Qin *et al* 2020, Meyer *et al* 2022, Ingham *et al* 2024) to prevent radiation damage to healthy organs. Preclinical imaging of TAT radionuclides and their surrogates can be conducted using SPECT (Koniar *et al* 2022, 2024), PET (Müller *et al* 2017), PET-SPECT (Goorden *et al* 2013, Beekman *et al* 2021) or a Compton camera (Das *et al* 2025) depending on the type of emissions and resolution requirements.

Successful utilization of different emissions jointly has been attempted previously across a diverse range of imaging modalities: (i) JR of ^{90}Y from the continuous bremsstrahlung spectrum in SPECT (Chun *et al* 2020), (ii) projection-domain based dose quantification for ^{227}Th and ^{223}Ra in SPECT (Li *et al* 2024), (iii) joint utilization of 'PET events' and 'Compton events' in Compton-PET (Ghosh and Das 2023, Takyu *et al* 2025), and (iv) JR of different channels of information for a multi-layer Compton camera used in online beam range verification based on prompt gamma imaging (Roser *et al* 2022).

In this work, we compare three JR schemes to simultaneously use two photopeaks from radionuclides emitting multiple gammas and/or positrons. We tested these algorithms with simulations representing the preclinical PET-SPECT VECTor scanner (Goorden *et al* 2013) (MILabs B.V.). The VECTor scanner of which the initial version was introduced in 2013, equipped with clustered pinhole technology (Beekman 2011), experimentally demonstrates sub-millimeter resolutions at 140 keV of ^{99m}Tc (Goorden *et al* 2013), 364 keV of ^{131}I (van der Have *et al* 2016), 440 keV of ^{213}Bi (de Swart *et al* 2016), 511 keV of ^{18}F (Goorden *et al* 2013), 603 keV of ^{124}I and 909 keV of ^{89}Zr (Beekman *et al* 2021) and, according to simulations, can also achieve sub-millimeter resolution for ultra-high energy (>1 MeV) prompt gammas up till 1.4 MeV (Ghosh *et al* 2025), making it a suitable modality for imaging all radionuclides listed in table 1, which emit gammas across a broad energy range. Additionally, the scanner is capable of performing positron range-free PET and multi-tracer PET imaging (Beekman *et al* 2021).

For this study, we performed Monte Carlo simulations for ^{225}Ac, ^{226}Ac and ^{89}Zr activity distributions to characterize the proposed methods for a wide energy range of 158 keV to 909 keV. Derenzo resolution phantom images at different activity concentrations were assessed for each radionuclide and quantitatively compared via a contrast-to-noise (CNR) analysis.

2. Materials and methods

2.1. Scanner description

We simulated the VECTor PET-SPECT scanner (Goorden *et al* 2013, Beekman *et al* 2021) with standard crystal thickness to evaluate our algorithms. The detector component of this scanner consists of three, triangularly arranged, monolithic NaI(Tl) scintillator detectors (9.5 mm thick) with PMT-based light collection. Each individual planar detector has a surface area of 497 × 411 mm^2 (Van Der Have *et al* 2009). The collimator employed in this study is designed based on proprietary cluster collimation technology (Beekman 2011) and consists of 48 clusters, each containing 2 × 2 pinholes, resulting in a total of 162 knife-edge pinholes. The cylindrical collimator has an inner diameter of 48 mm, and a wall thickness of 43 mm. The centers of all pinholes are positioned at a 64 mm diameter. The pinholes are organized into four adjacent rings in longitudinal direction, with those in the inner two rings having an opening angle of 18°, while the pinholes in the outer two rings have an opening angle of 16°. The collimator is made of a material mixture consisting of tungsten (97%), nickel (1.5%), and iron (1.5%).

The central field of view (CFOV) is the region sampled collectively by all pinholes. In the CFOV complete data sampling is thus achieved in accordance with Tuy's condition without any bed movement (Tuy 1983). For imaging objects larger than the CFOV, data acquisition is performed using the scanning focus method (Vastenhouw and Beekman 2007), where the sample-holding bed is incrementally translated in a finite number of steps, and the data acquired from all bed positions is used simultaneously to reconstruct the 3D tracer distribution.

2.2. Monte Carlo simulations

2.2.1. Scanner simulation and data acquisition

Monte Carlo (MC) simulations were performed using GATE v9.0 (Jan *et al* 2004), which is based on Geant4 v10.05 (Agostinelli *et al* 2003) and ran on a CentOS 7.0 cluster. The three NaI(Tl) planar detectors were modeled in the GATE environment as three rectangular boxes of dimensions 497 × 411 × 9.5 mm^3. The first detector was positioned perpendicular to the y-axis and translated to the coordinates (0, −215 mm, 0). The second and third detectors were rotated by ±120° around the z-axis and translated to the positions (−186 mm, −107 mm, 0) and (186 mm, −107 mm, 0), respectively, in order to precisely replicate the triangular configuration of the VECTor scanner (figure 1). The clustered pinhole collimator was simulated according to the geometric parameters provided by the manufacturer, and its performance was validated on the VECTor scanner as reported in Goorden *et al* (2013). Three radionuclides—^{225}Ac, ^{226}Ac and ^{89}Zr—were used in this study. GATE's 'ion source' utility was used to simulate all types of emissions from these radionuclides. The selection of these radionuclides was motivated by their relevance to current applications and the opportunity to evaluate the proposed JR methods using gamma emissions across different energy ranges. The lower energy range includes 158, 218, 230, and 440 keV emissions from ^{225}Ac and ^{226}Ac, while the higher energy range includes 511 and 909 keV emissions from ^{89}Zr. Additionally, these radionuclides offer varying degrees of proximity between gamma energies from individual radionuclides. For instance, ^{226}Ac provides closely spaced gamma emissions at 158 and 230 keV. ^{225}Ac exhibits more widely separated gamma lines at 218 and 440 keV, while ^{89}Zr results in a larger energy spacing with 909 keV gammas and 511 keV annihilation photons. Physics processes were built using the 'emstandard' physics list builder (see GATE documentation). Photomultipliers, light collection and back-end electronics of the scanner were not modeled.

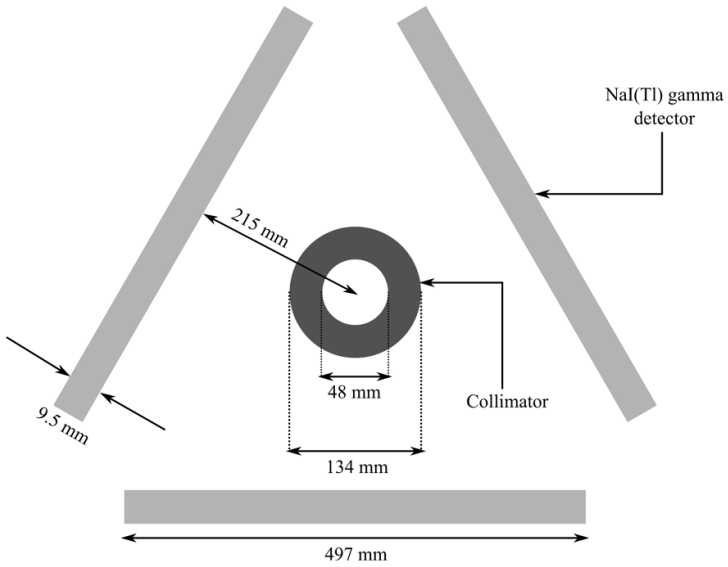

Figure 1. Transaxial view of the VECTor scanner equipped with a clustered pinhole collimator, illustrating the geometrical dimensions (detector thickness not to scale).

Table 2. Comparing experimental energy resolution (ER) values with simulated ones.

Source	Energy (keV)	Experimental ER (%)	Simulated ER (%)
^{125}I	35	22.7 (Villena *et al* 2010)	20.0$^{(a)}$
^{99m}Tc	140	10.0 (Villena *et al* 2010)	10.0$^{(a)}$
^{22}Na	511	9.7 (Villena *et al* 2010)	9.0$^{(b)}$
^{124}I	603	8.3 (Beekman *et al* 2021,Nguyen *et al* 2020)	8.3$^{(b)}$
^{89}Zr	909	7.2 (Beekman *et al* 2021,Ghosh *et al* 2025)	6.8$^{(b)}$

Abbreviations: ER$^{(a)}$ for model-A and ER$^{(b)}$ for model-B.

Rather, their aggregate effect is replicated by modeling 10% energy resolution (ER) at 140 keV for ^{225}Ac and ^{226}Ac simulations and 9% ER at 511 keV for ^{89}Zr, as per the manufacturer's specifications. For both cases, $\frac{1}{\sqrt{E}}$ scaling was considered individually from a 140 keV energy (model-A) for ^{225}Ac and ^{226}Ac and from a 511 keV energy (model-B) for ^{89}Zr to simulate the ER at different gamma energies such that it matches well with experimentally determined ERs (table 2). Also, a 3.5 mm FWHM intrinsic spatial resolution of the detector was assumed, as per manufacturer's specifications. These resolutions were implemented by sampling from Gaussian distributions with respective FWHMs. Natural background (NB), corresponding to the detector counts present in the absence of activity, was also included to improve realism. A count rate of 1 keV^{-1} s^{-1} was assumed for each of the three planar detectors of the VECTor scanner, in accordance with the manufacturer's specifications. This count rate was used to generate Poisson distributed NB across all three detector planes. Finally, gamma detection positions on the detector surface were discretized in 1.072 $\times$ 1.072 mm^2 pixels to obtain projection data. All of these post processing tasks were implemented through MATLAB v2021b scripts.

2.2.2. Digital phantoms

For ^{225}Ac, two different Derenzo resolution phantoms and three different activity concentrations were utilized in the study. For a concentration of 20 MBq ml^{-1}, a Derenzo phantom with rod diameters of 0.75, 0.7, 0.65, 0.6, 0.55, and 0.5 mm, each with a length of 10 mm, was employed (figure 2). These rods were positioned within a PMMA cylinder with a diameter of 12 mm and a height of 12 mm. We name this phantom DP-1. The activity concentration of 20 MBq ml^{-1} exceeds the values typically encountered in biological experiments for this radionuclide (appendix A.1). Nevertheless, this concentration was investigated to characterize the proposed JR methods in the SPECT energy range. For the other two activity concentrations of 0.5 MBq ml^{-1} and 0.2 MBq ml^{-1}, a different Derenzo phantom with rod diameters of 1.6, 1.5, 1.4, 1.1, 1.0, and 0.9 mm and a rod length of 10 mm was used suitable for the changed reconstructed rod visibility. The hot rods were housed within a PMMA cylinder with a diameter of 20 mm and a height of 12 mm. We name this phantom DP-2.

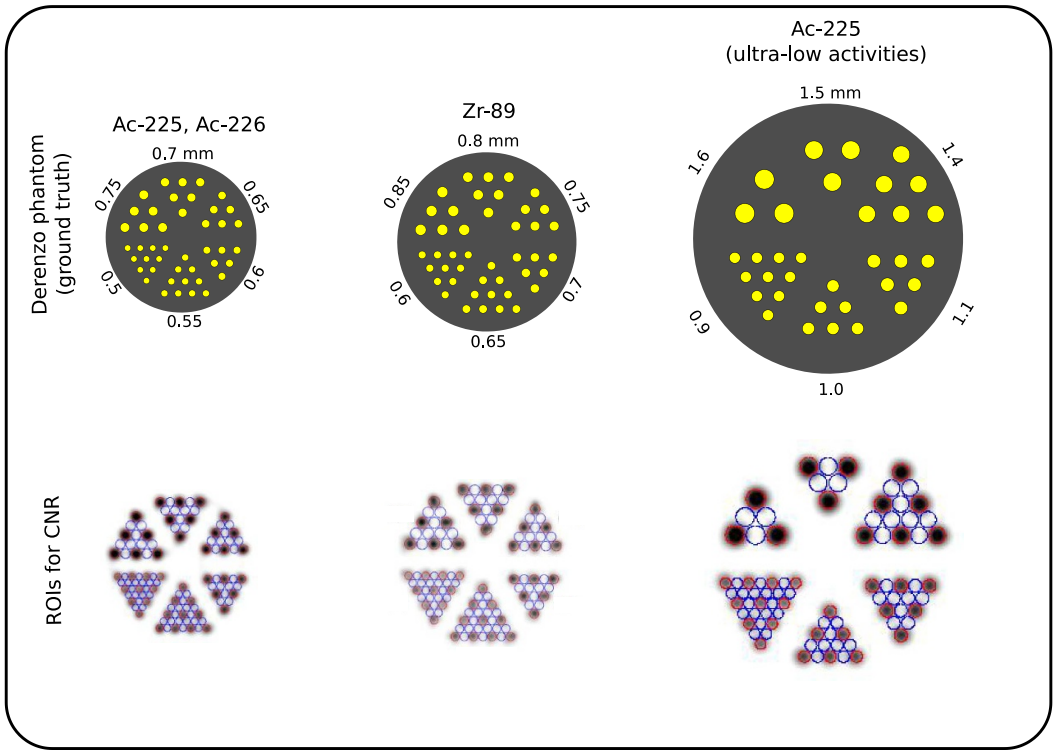

Figure 2. Ground truth representation of Derenzo resolution phantoms embedded within a PMMA cylinders (in gray) having diameters of 12 mm, 14 mm, and 20 mm (left to right), with rod diameters indicated in the top row. Respective ROI placements for CNR calculation are shown in the second row.

For ^{226}Ac, the above described DP-1 phantom was used with activity concentrations kept at 10 MBq ml^{-1}, 2 MBq ml^{-1}, and 1 MBq ml^{-1}.

For ^{89}Zr, a Derenzo resolution phantom with rod diameters of 0.85, 0.8, 0.75, 0.7, 0.65, and 0.6 mm and a rod length of 10 mm was employed, named DP-3 (figure 2). These rods were enclosed within a PMMA cylinder with a diameter of 14 mm and a height of 12 mm. Activity concentrations of 200 MBq ml^{-1}, 100 MBq ml^{-1}, and 50 MBq ml^{-1} were investigated.

For all three radionuclides, the selection of activity concentrations was motivated to show degradation of resolution as activity concentration decreases, and to investigate benefit of proposed JR at these different levels of resolution degradation. For all cases, data acquisition was performed using a multi-planar trajectory (MPT) approach (Vaissier *et al* 2012) across 9 bed positions, with a total scan duration of 1 h.

2.2.3. Positron range simulation

The positron annihilation point distribution was calculated for ^{89}Zr using a MC simulation of a point source placed at the center of a 20 cm water sphere. A total of five million positron annihilation events were simulated. The three-dimensional coordinates of the annihilation points were recorded on a $31 \times 31 \times 31$ voxel grid, where the central voxel corresponded to the position of the point source. The voxel size was the same as in the corresponding reconstructed images. The resulting positron range kernel was subsequently normalized.

2.3. JR schemes

In this paper we describe and validate the joint reconstruction schemes for two photopeaks. However, the extension to more photopeaks is in principle straightforward, though such schemes will have added computational complexity. Note that for the isotopes considered in this paper, there are only two photopeaks with reasonable intensity.

Consider a radionuclide emitting gamma photons of two energies E_1 and E_2 of intensities $I_1\%$ and $I_2\%$ respectively. We assume that these two energies are sufficiently separated so that the different photopeaks can be resolved by the scanner. We define $a \in R^N$ as a vector representing the amount of activity in the N voxels in the object. Let $p^{(1)} \in R^V$ and $p^{(2)} \in R^V$ denote the noiseless projections

from the two emissions corresponding to gamma photons of energy E_1 and E_2 respectively. Here, V is the total number of pixels of the detectors, multiplied by the number of bed positions utilized in the scan (see section 2.1). Also, let $s^{(1)} \in R^V$ and $s^{(2)} \in R^V$ be estimated noiseless scatter projections (for scattered gammas detected in the photopeak) which depend on the activity distribution. Furthermore, $M^{(1)} \in R^{V\times N}$ and $M^{(2)} \in R^{V\times N}$ are energy dependent system matrices describing photon transport for gamma energies E_1 and E_2 respectively. These matrices exclude scatter but include gamma photon penetration through collimator and in the detector.

In image reconstruction, we use an ordered-subset based maximum likelihood expectation maximization algorithm (see section 2.4 for specific implementation details). This algorithm includes forward projection/ backprojection steps in each sub-iteration which are implemented in different ways for the different separate and JR schemes that we compare. This is detailed below given the earlier defined quantities for the forward projection step in the algorithm. For the backprojection step, the same equation but without the scatter component is used.

2.3.1. Separate reconstruction of photopeaks

The conventional method for formulating the problem is to treat projections from different gamma energies independently which would result in separate images for each photopeak. Accordingly, the relation between noiseless projection and activity in the forward projection step of iterative image reconstruction can be written as

$$\begin{pmatrix} p_1^{(i)} \\ p_2^{(i)} \\ .. \\ .. \\ p_V^{(i)} \end{pmatrix}_{V\times 1} = \tau_i \begin{pmatrix} m_{11}^{(i)} & m_{12}^{(i)} & .. & .. & m_{1N}^{(i)} \\ m_{21}^{(i)} & m_{22}^{(i)} & .. & .. & m_{2N}^{(i)} \\ .. & .. & .. & .. & .. \\ .. & .. & .. & .. & .. \\ m_{V1}^{(i)} & m_{V2}^{(i)} & .. & .. & m_{VN}^{(i)} \end{pmatrix}_{V\times N} \begin{pmatrix} a_1 \\ a_2 \\ .. \\ .. \\ a_N \end{pmatrix}_{N\times 1} + \begin{pmatrix} s_1^{(i)} \\ s_2^{(i)} \\ .. \\ .. \\ s_V^{(i)} \end{pmatrix}_{V\times 1} \tag{1}$$

where $\tau_i =$ factors convert activity into emitted counts for respective energies (here, $T_{1/2}$: half life of the radionuclide; t: scan time) and system matrix element $[m_{vn}^{(i)}]$ is defined as the probability of a gamma photon of energy E_i emitted from the nth voxel to get detected in the vth detector pixel.

2.3.2. Post combining images

Activity distribution estimates obtained from separate reconstructions of two gamma energies (section 2.3.1) can be combined (added) to generate an additional estimate.

2.3.3. Single-band (SB) JR

One approach of combining the two projection equations in equation (1) is as follows

$$\begin{pmatrix} p_1^{(1)} + p_1^{(2)} \\ p_2^{(1)} + p^{(2)} \\ .. \\ .. \\ p_V^{(1)} + p_V^{(2)} \end{pmatrix}_{V\times 1} = \begin{pmatrix} m_{11}^{ave} & m_{12}^{ave} & .. & .. & m_{1N}^{ave} \\ m_{21}^{ave} & m_{22}^{ave} & .. & .. & m_{2N}^{ave} \\ .. & .. & .. & .. & .. \\ .. & .. & .. & .. & .. \\ m_{V1}^{ave} & m_{V2}^{ave} & .. & .. & m_{VN}^{ave} \end{pmatrix}_{V\times N} \begin{pmatrix} a_1 \\ a_2 \\ .. \\ .. \\ a_N \end{pmatrix}_{N\times 1} + \begin{pmatrix} s_1^{(1)} + s_1^{(2)} \\ s_2^{(1)} + s_2^{(2)} \\ .. \\ .. \\ s_V^{(1)} + s_V^{(2)} \end{pmatrix}_{V\times 1} \tag{2}$$

where $[m_{ij}^{\text{ave}}]$ is a system matrix element at weighted average energy

$$E_{\text{ave}} = \frac{I_1E_1 + I_2E_2}{I_1 + I_2}. \tag{3}$$

The photon transport model for two gamma energies, when implemented in this manner in image reconstruction, is referred to as (SB-JR).

2.3.4. Mixed multi-band (mMB) modeling JR

Another way to combine photon transport into a joint equation is to include photon transport in the system matrix by element-wise summation of the matrix elements for the two energies

$$\begin{pmatrix} p_1^{(1)}+p_1^{(2)} \\ p_2^{(1)}+p_2^{(2)} \\ .. \\ .. \\ p_V^{(1)}+p_V^{(2)} \end{pmatrix}_{V\times 1} = \begin{pmatrix} \tau_1 m_{11}^{(1)}+\tau_2 m_{11}^{(2)} & \tau_1 m_{12}^{(1)}+\tau_2 m_{12}^{(2)} & .. & .. & \tau_1 m_{1N}^{(1)}+\tau_2 m_{1N}^{(2)} \\ \tau_1 m_{21}^{(1)}+\tau_2 m_{21}^{(2)} & \tau_1 m_{22}^{(1)}+\tau_2 m_{22}^{(2)} & .. & .. & \tau_1 m_{2N}^{(1)}+\tau_2 m_{2N}^{(2)} \\ .. & .. & .. & .. & .. \\ .. & .. & .. & .. & .. \\ \tau_1 m_{V1}^{(1)}+\tau_2 m_{V1}^{(2)} & \tau_1 m_{V2}^{(1)}+\tau_2 m_{V2}^{(2)} & .. & .. & \tau_1 m_{VN}^{(1)}+\tau_2 m_{VN}^{(2)} \end{pmatrix} \begin{pmatrix} a_1 \\ a_2 \\ .. \\ .. \\ a_N \end{pmatrix}_{N\times 1} + \begin{pmatrix} s_1^{(1)}+s_1^{(2)} \\ s_2^{(1)}+s_2^{(2)} \\ .. \\ .. \\ s_V^{(1)}+s_V^{(2)} \end{pmatrix}_{V\times 1} . \tag{4}$$

This approach for incorporating the photon transport model into image reconstruction is termed (mMB-JR).

2.3.5. Multi-band (MB) modeling JR

In the above formulations we considered the total number of gammas detected in the two photopeak windows (projections were added). Simply adding projections means that information about the energy of the detected gamma is lost. We therefore consider a third formulation in which this information is retained.

$$\begin{pmatrix} \begin{pmatrix} p_1^{(1)} \\ p_2^{(1)} \\ .. \\ .. \\ p_V^{(1)} \end{pmatrix}_{V\times 1} \\ \begin{pmatrix} p_1^{(2)} \\ p_2^{(2)} \\ .. \\ .. \\ p_V^{(2)} \end{pmatrix}_{V\times 1} \end{pmatrix}_{2V\times 1} = \begin{pmatrix} \tau_1 \begin{pmatrix} m_{11}^{(1)} & m_{12}^{(1)} & .. & .. & m_{1N}^{(1)} \\ m_{21}^{(1)} & m_{22}^{(1)} & .. & .. & m_{2N}^{(1)} \\ .. & .. & .. & .. & .. \\ .. & .. & .. & .. & .. \\ m_{V1}^{(1)} & m_{V2}^{(1)} & .. & .. & m_{VN}^{(1)} \end{pmatrix}_{V\times N} \\ \tau_2 \begin{pmatrix} m_{11}^{(2)} & m_{12}^{(2)} & .. & .. & m_{1N}^{2} \\ m_{21}^{(2)} & m_{22}^{(2)} & .. & .. & m_{2N}^{(2)} \\ .. & .. & .. & .. & .. \\ .. & .. & .. & .. & .. \\ m_{V1}^{(2)} & m_{V2}^{(2)} & .. & .. & m_{VN}^{(2)} \end{pmatrix}_{V\times N} \end{pmatrix}_{2V\times N} \begin{pmatrix} a_1 \\ a_2 \\ .. \\ .. \\ a_N \end{pmatrix}_{N\times 1} + \begin{pmatrix} \begin{pmatrix} s_1^{(1)} \\ s_2^{(1)} \\ .. \\ .. \\ s_V^{(1)} \end{pmatrix}_{V\times 1} \\ \begin{pmatrix} s_1^{(2)} \\ s_2^{(2)} \\ .. \\ .. \\ s_V^{(2)} \end{pmatrix}_{V\times 1} \end{pmatrix}_{2V\times 1} \tag{5}$$

We thus kept the two projections and their system matrices at the cost of doubling the computation time for reconstruction as the dimension of the equation doubled. Implementing this photon transport model into image reconstruction is denoted by (MB-JR).

2.4. Image reconstruction

Image reconstructions were performed using the dual-matrix dual-voxel similarity-regulated ordered-subset expectation maximization (DM-DV) algorithm (Goorden *et al* 2020), with similarity threshold value set to 40% (Vaissier *et al* 2016). Pixel-based ordered subsets (Branderhorst *et al* 2010) were used for acceleration of reconstruction. For the DP-1 phantom (high-count ^{225}Ac and ^{226}Ac), a voxel size of 0.2 mm was used, due to the smallest rod diameter being 0.5 mm. A 3D Gaussian post-filter with FWHM values of 0.5 mm was applied. For DP-2 phantom (low-count ^{225}Ac), the voxel size was 0.4 mm,

chosen because the smallest rod diameter is 0.9 mm. 3D Gaussian post-filters of 1.0 mm and 1.4 mm FWHM were used for the DP-2 phantom at activity concentrations 0.5 MBq ml^{-1} and 0.2 MBq ml^{-1}, respectively. For the DP-3 phantom (^{89}Zr), a voxel size of 0.4 mm was used in the reconstruction process. A 3D Gaussian filter with a FWHM of 0.5 mm was applied. The filter widths were selected to be approximately equal to the diameter of the smallest visible sector, except for ^{89}Zr, for which a value of 0.5 mm was chosen to enable comparison with the results reported by Ghosh *et al* (2025).

For improved visualization, the 20 central slices of the DP-1 phantom and 10 central slices of the DP-2 and the DP-3 phantom were summed, and the resulting images were resampled to a finer grid of 256 × 256 using MATLAB's 'resize' function.

2.4.1. System matrices

Energy-dependent system matrices ($M^{(1)}, M^{(2)}$ of section 2.3) were generated using in-house developed ray-tracing software (Goorden *et al* 2011, 2016). This ray-tracer accounts for attenuation through the collimator and detector, but does not incorporate scatter. Instead, scatter projections ($s^{(1)}, s^{(2)}$ of section 2.3) were estimated from side energy windows using the triple-energy window (TEW) scatter correction method (Ogawa *et al* 1991) and were then used as additive term only in forward projection. Attenuation and scatter within the small animal body were not modeled in the system matrix due to the relatively small size of mice.

In accordance with the DM method, cutoffs of 1% and 20% were applied to generate the forward and backprojection matrices, respectively, to accelerate the reconstruction process by using a smaller backprojection matrix. Here, 1% cutoff implies that gamma rays with less than a 1% chance of penetrating the collimator were excluded (Goorden *et al* 2020). Furthermore, the forward matrix was divided into central and tail components. The PSF exhibits a rapidly varying central component and a slowly varying tail component on the detector plane (see figure 2 of Goorden *et al* (2016)). Since the tail component varies slowly, it was defined using coarser voxels; these were twice the size as those used for the central component. This DV approach effectively reduces both storage requirements for the system matrix and computational load during reconstruction. Note that both the described matrix generation method and the reconstruction acceleration correspond to what is used in the experimental system.

For imaging single photopeaks from each radionuclide, system matrices at the respective energies with 128 subsets were used. For SB-JR, a system matrix at intensity weighted energy value (equation (2)) was used where the total number of subsets was 128. The intensity weighted energy values are 374 keV, 207 keV, and 784 keV for ^{225}Ac, ^{226}Ac, and ^{89}Zr, respectively. In mMB-JR, a total of 128 subsets were used with matrix elements added (equation (4)). For MB-JR, there are a total of 256 subsets, of which the first 128 correspond to the lower gamma energy, while the remaining 128 correspond to the higher gamma energy (equation (5)). A comparison of imaging performance due to different schemes of energy subsetting is presented in appendix A.2.

Among the three radionuclides under investigation, ^{225}Ac exhibits gamma emissions at 218 keV (11%) and 440 keV (26%) that do not originate directly from the radionuclide itself; rather, these emissions are produced by its daughter nuclides, ^{221}Fr and ^{213}Bi, respectively. Nevertheless, the corresponding intensities of 11% and 26% are utilized for the $[\tau_i$ calculation (section 2.3.1) without applying any correction. This is justified because of the shorter half-lives of ^{221}Fr (4.8 min) and ^{213}Bi (45.6 min) compared to ^{225}Ac (10 d), which allows the decay chain to reach transient equilibrium (Robertson *et al* 2017).

2.4.2. Positron range correction

For imaging 511 keV gammas resulting from positron decay of ^{89}Zr, the positron range was included in the system matrix. Consider $M^{511} \sim= \left[m_{ij}^{511}\right] \in R^{V\times N}$ being the system matrix for single gammas with an energy of 511 keV and $K^{\mathrm{PR}} \sim= \left[h_j\right] \in R^{Q}$ being the column matrix representation of the positron range kernel calculated as explained in section 2.2.3, with Q equals to total number of entries in the column matrix. Then, the corresponding system matrix $M^{511(\mathrm{PR})} \sim= \left[m_{ij}^{511(\mathrm{PR})}\right] \in R^{V\times N}$, including positron range can be written as

$$m_{ij}^{\mathrm{PR}} = \sum_{r=1}^{Q} 2h_r m_{i\left(j+r-\frac{Q+1}{2}\right)}, \tag{6}$$

where the factor 2 is due the consideration that each positron emission results into approximately two annihilation photons.

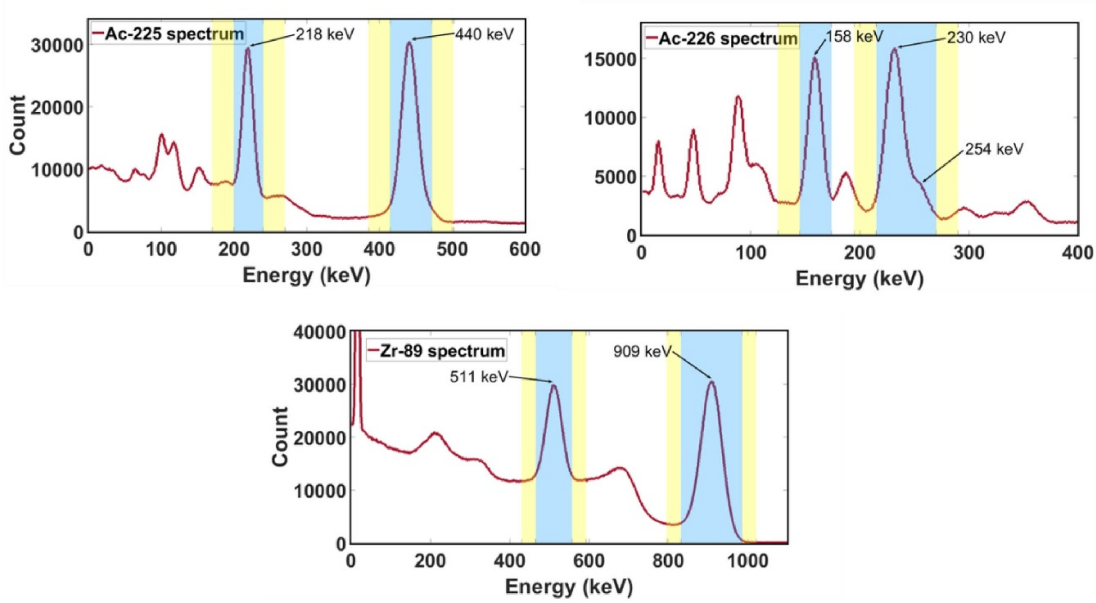

Figure 3. Energy spectra of the three radionuclides under study: ^{225}Ac, ^{226}Ac and ^{89}Zr, including the photopeak and background energy windows in blue and yellow, respectively.

2.5. Data analysis

A quantitative comparison of resolution phantom images generated from the different JR methods and from individual photopeaks was conducted using CNR analysis. For the CNR analysis, circular regions-of-interests (ROIs) were drawn on the filtered and finer sampled images of the Derenzo phantom (section 2.4), with their placements aligned to the Derenzo rods and the spaces in between (figure 2). The diameters of these ROIs were set to 0.9 times those of the corresponding rod sectors. These ROIs were applied to 20 central layers (axial direction) of the DP-1 and 10 central layers (axial direction) of the DP-2 and DP-3 phantoms. If $\bar{h}$ is the average activity (over all axial layers) in ROIs corresponding to rods of diameter d and similarly $\bar{b}$ is the average background activity for the in-between ROIs, then contrast for that rod sector is given by

$$C_d = \frac{\bar{h} - \bar{b}}{\bar{b}}. \tag{7}$$

Noise for that rod sector is then defined as

$$N_d = \frac{\sqrt{\sigma_h^2 + \sigma_b^2}}{\bar{h} + \bar{b}} \tag{8}$$

where σ_h and σ_b are standard deviations for ROIs corresponding to Derenzo rods and in between ROIs respectively. CNR for a rod sector is defined as a ratio between contrast and noise.

$$\mathrm{CNR}_d = \frac{C_d}{N_d}. \tag{9}$$

For statistical accuracy, CNR was calculated over three noise realizations.

3. Results

3.1. Phantom simulation

The energy spectra for radionuclides ^{225}Ac and ^{226}Ac were generated using the first 5 min of the GATE simulations of the highest activity concentrations used in this work (20 MBq ml^{-1} for ^{225}Ac and 10 MBq ml^{-1} for ^{226}Ac). Similarly, the energy spectrum for ^{89}Zr was produced using the first minute of the simulated acquisition for the activity concentration of 200 MBq ml^{-1}. These spectra are presented in figure 3, where the photopeak and background energy windows are indicated in blue and yellow, respectively. The exact values of these energy windows are provided in table 3.

Table 3. Photopeak and background windows used for three radionuclides under study.

Radionuclide	Peak energy (keV)	Photopeak window (keV)	Background window-1 (keV)	Background window-2 (keV)
^{225}Ac	218	200–240	170–200	240–270
	440	415–472	385–415	472–502
^{226}Ac	158	145–174	125–145	195–215
	230 + 254	215–270	195–215	270–290
^{89}Zr	511	465–557	430–465	557–592
	909	831–986	796–831	986–1021

The photopeak energy windows were selected 'by hand' to include nearby gamma emissions where feasible. For instance, the 230 keV and 254 keV gamma emissions of ^{226}Ac were combined within a single photopeak window, and the center of the peak was defined as the intensity-weighted mean energy of 231 keV, which was used for system matrix calculation. The widths of the background energy windows were maximized while excluding nearby low intensity gamma emissions. This approach aimed to minimize noise propagation from side windows in the TEW scatter correction (Ogawa *et al* 1991), which was particularly important when working with low and ultra-low activity levels.

3.2. Derenzo phantom studies

The 30th and 90th iterations of the ^{225}Ac resolution phantom images generated by using individual gamma emissions, by post-combining these after reconstruction, and by the proposed three JR methods are presented in figure 4 for all studied activity concentrations.

Images obtained from the 440 keV photopeak exhibit lower quality compared to all other five methods. At an activity concentration of 20 MBq ml^{-1}, MB-JR produces slightly superior images compared to the 218 keV photopeak images, and markedly superior images relative to the 440 keV photopeak images, the post-combined images and the images obtained by the two other methods (mMB-JR and SB-JR). This improvement is evidenced by the enhanced peak-to-valley ratio observed in the line profiles (figure S1) and is further confirmed by the CNR-based quantitative analysis presented in section 3.3. In contrast, no improvement was observed for mMB-JR and SB-JR relative to 218 keV images.

At lower activity concentrations of 0.5 MBq ml^{-1} and 0.2 MBq ml^{-1}, images reconstructed using MB-JR are both visually and quantitatively superior to those from individual photopeaks and slightly outperform images from the other two. For mMB-JR and SB-JR, minor improvements were observed in the smallest visible sectors, while slight degradations occurred in larger rod sectors compared to the 218 keV photopeak images (see CNR plot in figure 7 and percentage improvements in figure 10). Line profiles through rods from the last visible rod sector—0.55 mm for 20 MBq ml^{-1}, 1.0 mm for 0.5 MBq ml^{-1}, and 1.4 mm for 0.2 MBq ml^{-1}—are shown in figure S1.

Notably, the benefit of independently including the two projections and their system matrices as done in the MB-JR scheme results in improved imaging performance compared to images obtained using the lower energy gamma, across all activity concentrations (see section 3.3). In contrast, other methods (SB-JR, mMB-JR) involve adding projection data and using an average gamma energy for the system matrix to reduce computational load which resulted in both improvements and slight degradations (only in larger rod sectors) in comparison to images obtained from lower energy gamma emissions.

Furthermore, it is evident that the strategy of adding images generated from two gamma emissions after individual reconstructions does not yield optimal images for none of the activity concentrations studied, highlighting the importance of utilizing JR methods.

Figure 5 presents ^{226}Ac images at activity concentrations of 10, 2, and 1 MBq ml^{-1}. Similar to observations for ^{225}Ac, the imaging performance achieved with the higher energy gamma emissions (230 + 254 keV) is inferior across all activity concentrations. For all activity concentrations examined, the JR methods produced images of superior quality compared to those obtained from individual photopeaks, with the exception of the 0.75 mm rod sector in SB-JR for 1 MBq ml^{-1} case; as confirmed by line profiles (figure S2), CNR analysis in section 3.3 and percentage improvements shown in figure 10. In the line profiles, rods from the outer edges of the respective last visible rod sector—0.55 mm for 10 MBq ml^{-1}, 0.6 mm for 2 MBq ml^{-1}, 0.7 mm for 1 MBq ml^{-1}—were shown for all cases (figure S2).

Similar to the ^{225}Ac case, the MB-JR method outperforms both SB-JR and mMB-JR in almost all cases (see figure 8). However, for ^{226}Ac, the performance differences among the three JR schemes are relatively small, as confirmed by the CNR analysis. One possible contributing factor to this may be

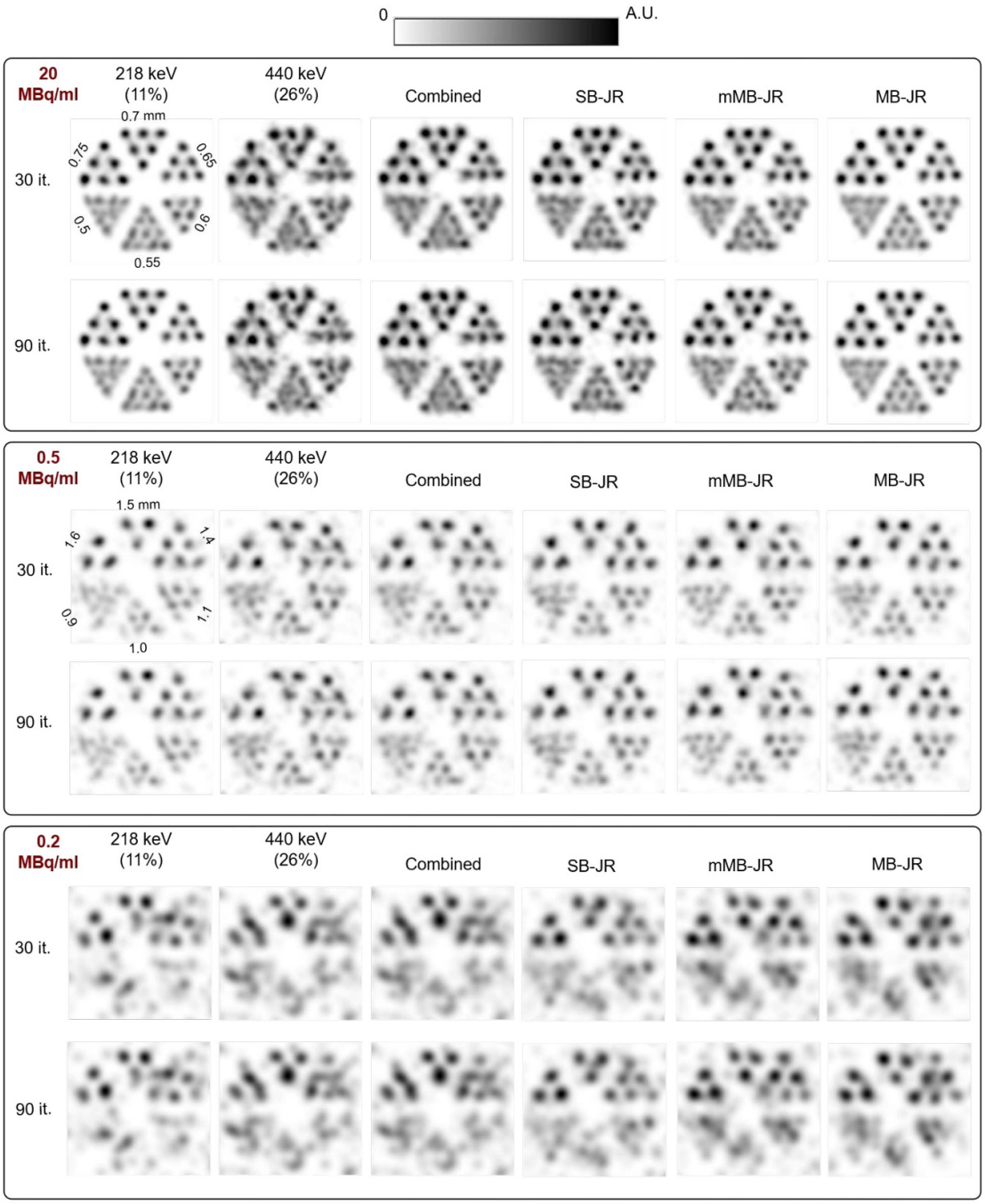

Figure 4. Derenzo resolution phantom images of ^{225}Ac after 30th and 90th iterations are shown for individual photopeaks (218 keV and 440 keV), two photopeak images combined after reconstruction, and three joint reconstruction schemes at three activity concentrations—20, 0.5 and 0.2 MBq ml^{-1}. Abbreviation: A.U., arbitrary unit.

the smaller separation between the gamma energies jointly reconstructed in this case (158 keV and 230 + 254 keV) compared to the more widely separated photopeaks of 218 keV and 440 keV in the ^{225}Ac case.

Figure 6 shows the 50th and 100th iterations of resolution phantom images—reconstructed using individual photopeaks, combining images after reconstruction and for three schemes of JRs—for ^{89}Zr at 200 MBq ml^{-1}, 100 MBq ml^{-1} and 50 MBq ml^{-1} activity concentrations. As observed with other radionuclides, reconstructions based on the higher energy gamma emission (909 keV) exhibit inferior image quality compared to all other images. Across all activity concentrations, the smallest discernible rod sectors demonstrate noticeable improvement when reconstructed using the proposed JR methods, as also confirmed by CNR analysis in section 3.3 and line profiles (figure S3). For larger rod sectors, the JR methods yield image quality comparable to that obtained from the lower energy gamma (511 keV).

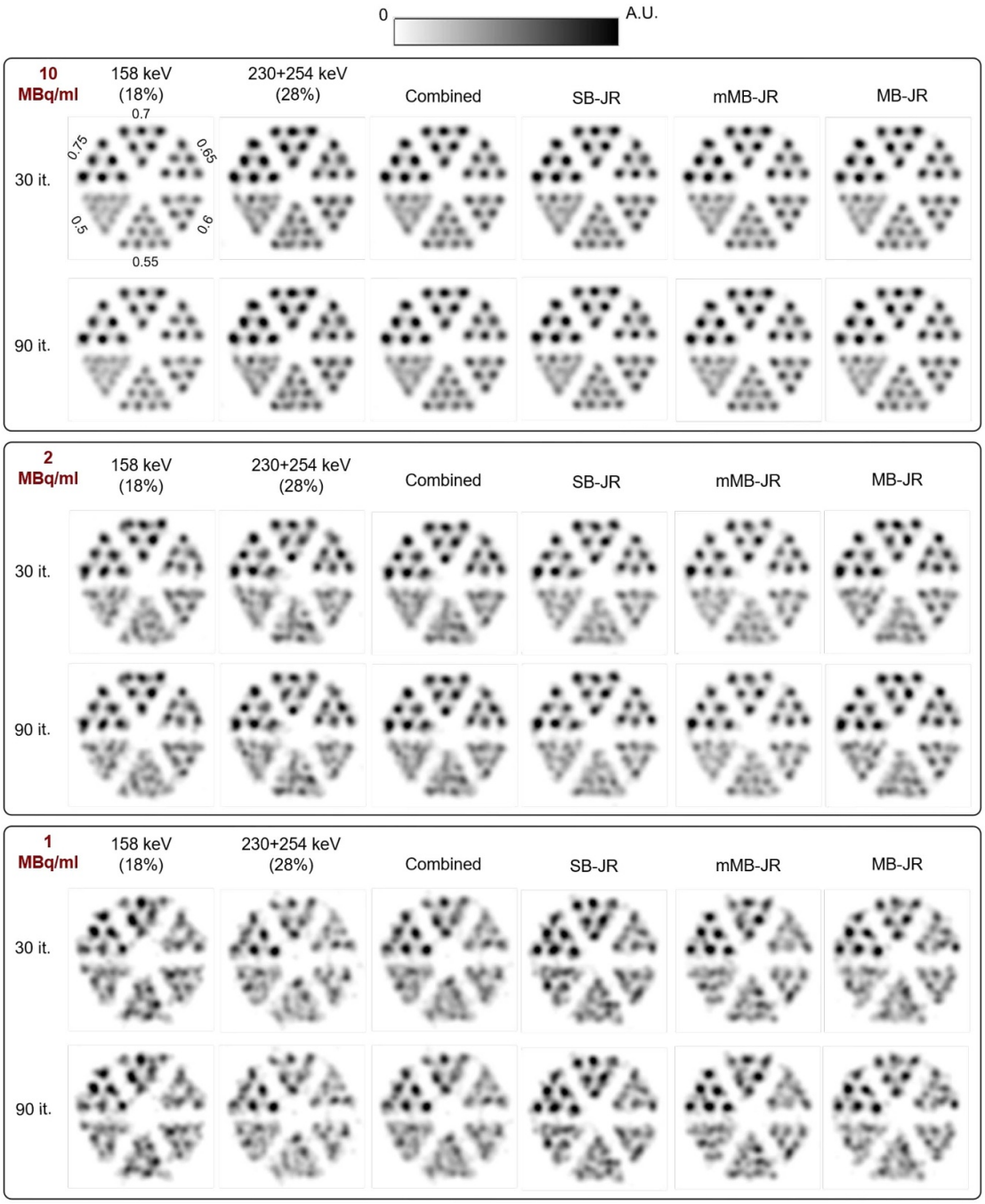

Figure 5. Derenzo resolution phantom images of ^{226}Ac after 30th and 90th iterations are shown for individual photopeaks (158 keV and 230 keV), two photopeak images combined after reconstructions, and three joint reconstruction schemes at three activity concentrations—10, 2 and 1 MBq ml^{-1}. Abbreviation: A.U., arbitrary unit.

Unlike the results observed in the lower energy range (158 keV—440 keV) for the other two radionuclides—where MB-JR consistently outperformed mMB-JR—in the higher energy range (511 keV—909 keV) we see comparable or even improved performance with mMB-JR relative to MB-JR. Notably, at 100 MBq ml^{-1}, the smallest rod sector (0.65 mm) is clearly visible using mMB-JR, whereas its visibility is compromised in the MB-JR reconstruction. This observation is supported by the CNR plots shown in figure 9(c) and the line profile (figure S3).

Finally, these results further confirm that post-combining images from two photopeak after reconstructions is not an effective approach, thereby additionally highlighting the advantages of JR methods for the higher energy range.

Furthermore, to investigate the runtime differences between the 128-subset and 256-subset reconstructions (section 2.4.1), we performed ^{226}Ac reconstructions on a computing node with 12 CPU

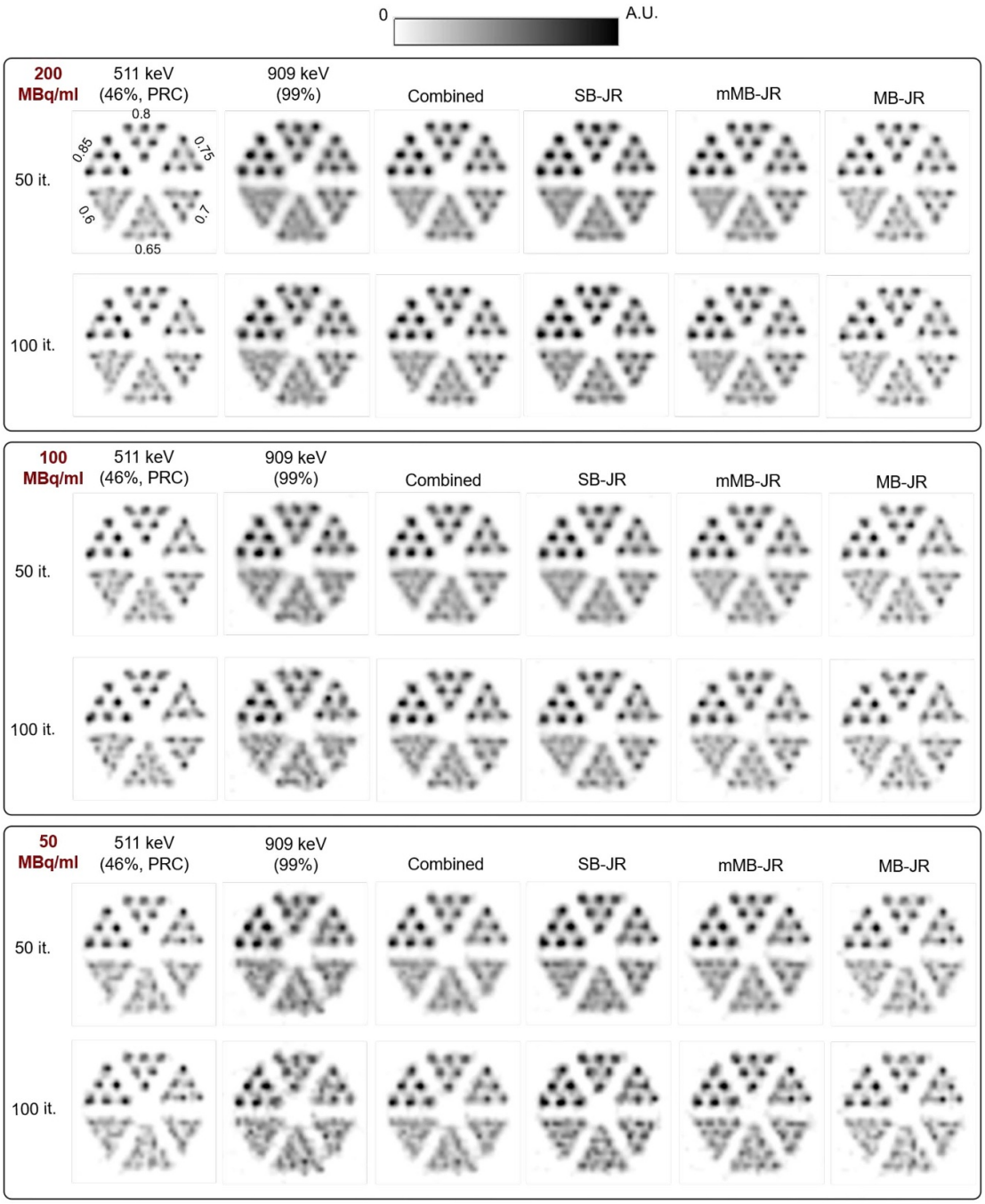

Figure 6. Derenzo resolution phantom images of ^{89}Zr after 50th and 100th iterations are shown for individual photopeaks (511 keV with PRC and 909 keV), two photopeak images combined after reconstructions, and three joint reconstruction schemes at three activity concentrations—200, 100 and 50 MBq ml^{-1}. Abbreviation: PRC, positron range correction; A.U., arbitrary unit.

Table 4. Runtimes (in hours) for 30 iterations of reconstructions using 128 subsets (158 keV, 230 keV, SB-JR, and mMB-JR) and 256 subsets (MB-JR).

Activity concentration	158 keV	230 keV	SB-JR	mMB-JR	MB-JR
10 MBq ml^{-1}	1.98	2.07	2.05	2.21	4.34
2 MBq ml^{-1}	1.69	1.81	1.84	2.02	3.74
1 MBq ml^{-1}	1.63	1.78	1.74	1.92	3.65

cores and 32 GB of memory of the same linux cluster used in this work (section 2.2.1). The jobs were executed with SINGLEJOB access policy to ensure exclusive node access and eliminate computational interference. The corresponding runtimes are presented in table 4.

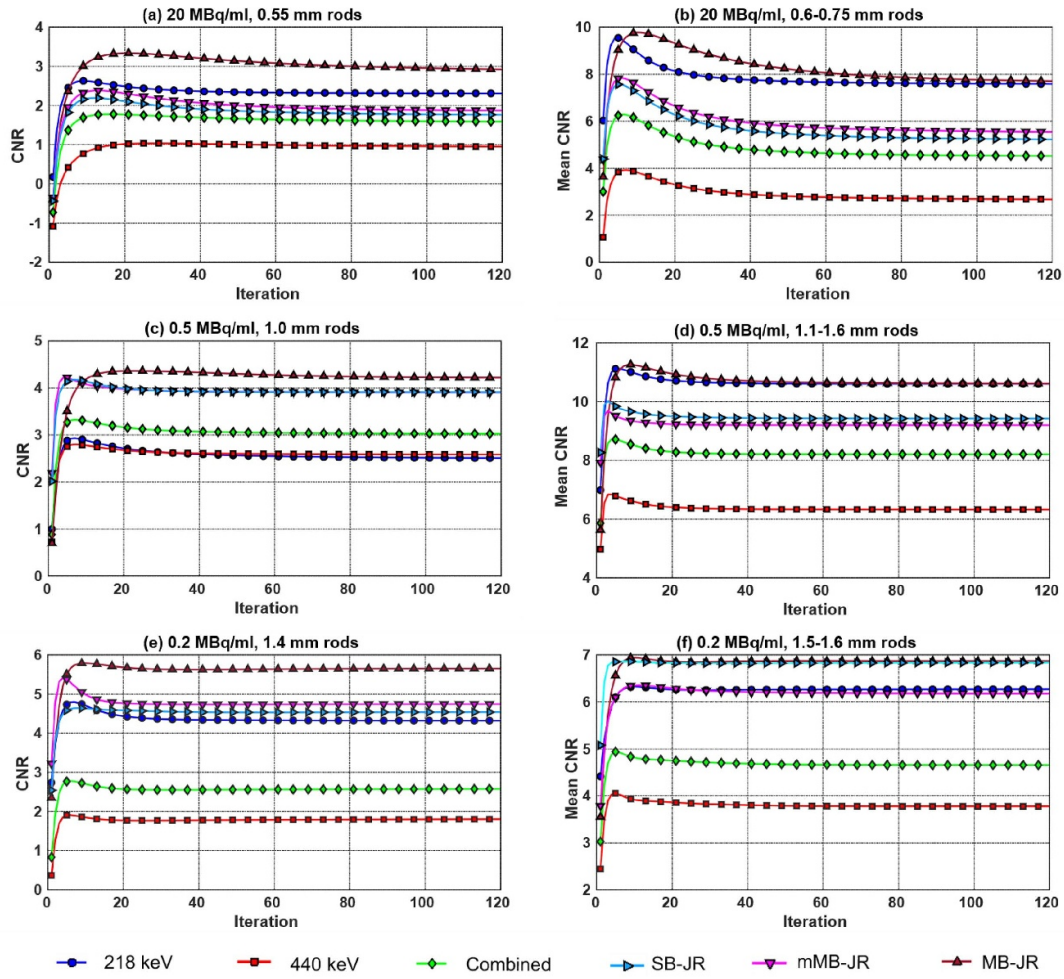

Figure 7. CNRs and mean CNRs of last visible sectors and rest of the visible sectors respectively (detailed on the y-axis and in the titles) are plotted against iteration number for all three different activity concentrations studied for ^{225}Ac. Abbreviation: SB-JR, **S**ingle-**B**and **J**oint **R**econstruction; mMB-JR, **m**ixed **M**ulti-**B**and **J**oint **R**econstruction; MB-JR, **M**ulti-**B**and **J**oint **R**econstruction.

3.3. CNR analysis

In addition to visual assessment of images and inspection of line profiles, a quantitative CNR analysis was conducted for all radionuclides under investigation, utilizing three noise realizations (figures 7–9). For each case, CNRs were calculated for the smallest discernible rod sectors (left column), and the mean CNRs of the remaining visible rod sectors were also provided (right column). It is noteworthy that the CNR improvements achieved by the MB-JR and mMB-JR schemes, relative to the respective lower-energy gamma emissions, are more pronounced for the smallest visible rod sectors than for the larger diameter rods, as reflected in the mean CNR values. Percentage improvement of CNR and mean CNR at the 60th (^{225}Ac, ^{226}Ac) and 100th (^{89}Zr) iterations for the three JR schemes over the best performing image for the individual photopeaks are reported in figure 10 with detailed data in tables S1–S3.

4. Discussion

Many SPECT and PET radionuclides have multiple detectable emissions with varying relative intensities and energies, sometimes affected by physical effects like positron range. Excluding certain emissions from the image-based diagnostics and therapies is not optimal especially in low-count scans. In this work, we proposed three types of JR algorithms which produce higher quality images compared to using single photopeaks. In general, this improvement is more enhanced as activity concentration is lowered. This may be attributed to the fact that increasing the signal-to-noise ratio, as JR incorporates information from both photopeaks, is most beneficial in low-count situations. Also, the enhancement from JR schemes is more pronounced for the smallest diameter visible sectors over larger rod sectors. This evidence suggests that in mouse scans, proposed JR methods may significantly enhance visibility and detectability of small and/or low-uptake lesions. Among the three methods MB-JR outperforms the

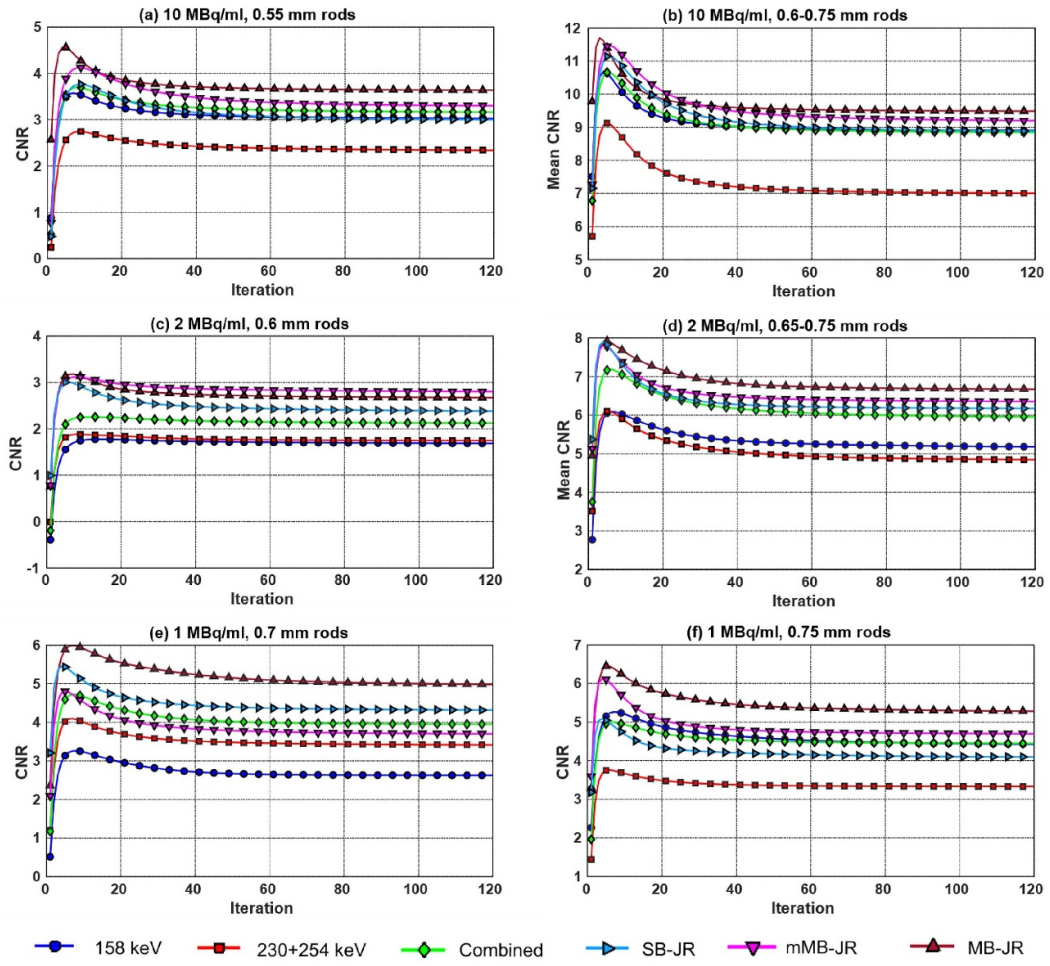

Figure 8. CNRs and mean CNRs of last visible sectors and rest of the visible sectors respectively (detailed on the y-axis and in the titles) are plotted against iteration number for all three different activity concentrations studied for ^{226}Ac. Abbreviation: SB-JR, **S**ingle-**B**and **J**oint **R**econstruction; mMB-JR, **m**ixed **M**ulti-**B**and **J**oint **R**econstruction; MB-JR, **M**ulti-**B**and **J**oint **R**econstruction.

other two—mMB-JR and SB-JR—in almost all cases at the cost of higher computational load. In mMB-JR and SB-JR, we added the counts from different photopeaks, as done in earlier studies (Dey *et al* 2014, Rowe *et al* 2015, Liu *et al* 2019, Ravizzini *et al* 2023), and, in contrast to previous works, we modeled the system matrix to include contributions from both gamma energies—element-wise in mMB-JR and using an average energy matrix in SB-JR.

Proposed methods can become beneficial for image-based dosimetry for TAT or TBT radionuclides considering the limit on total allowed injected activity (Nedrow *et al* 2017, Cheal *et al* 2020, Kelly *et al* 2020, Qin *et al* 2020, Meyer *et al* 2022, Ingham *et al* 2024). Many therapeutic radionuclides exhibit complex emission spectra (table 1), which can be imaged jointly using the proposed methods. As the focus on this work was on introducing the methodology rather than on optimizing imaging for a specific isotope, there are some limitations to our work. We did not consider the effects of alpha-recoil migration, meaning that the presented results for ^{225}Ac may overestimate the experimental outcome if this effect is not mitigated. The chemical detachment of alpha-emitting radionuclides from their carrier molecules because of alpha-recoil remains one of the major obstacles to the clinical application of TAT, as it can lead to unintended radiation dose to healthy tissues (De Kruijff *et al* 2015, 2019). Recently, encapsulation of alpha-emitters within nanocarriers has emerged as a promising strategy to mitigate the recoil problem, as such systems can retain daughter nuclides and thereby reduce off-target toxicity while preserving therapeutic efficacy (Sukthankar *et al* 2014, Holzwarth *et al* 2018, Majkowska-Pilip *et al* 2020, Muslimov *et al* 2021). The choice of ^{225}Ac was specifically motivated by the opportunity to evaluate the proposed JR approach using photopeaks at two widely separated energies (218 keV and 440 keV).

The lowest activity concentration of ^{225}Ac investigated in this study exceeds the currently available practical concentration range (estimated at 1–118 kBq ml^{-1}; appendix A.1). To evaluate the applicability of the proposed JR methods under lower activity levels, additional studies were conducted at activity

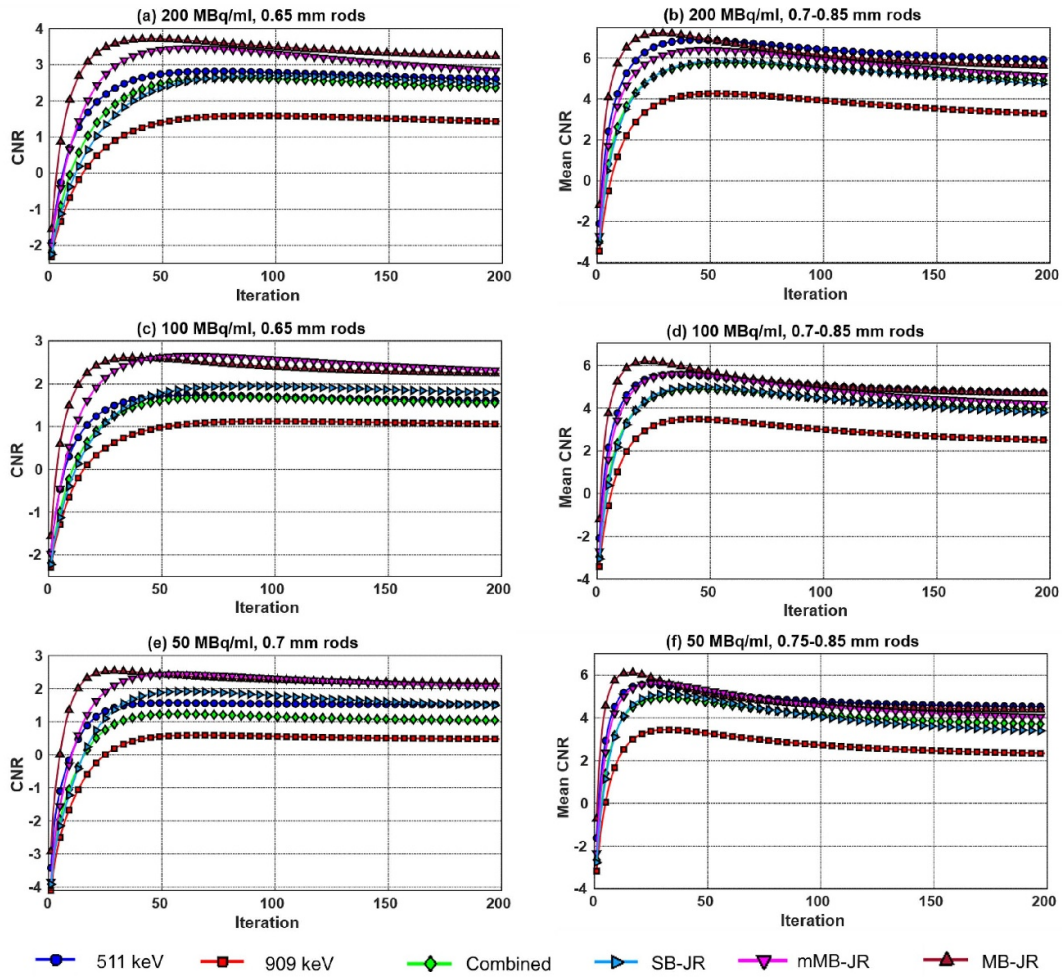

Figure 9. CNRs and mean CNRs of last visible sectors and rest of the visible sectors respectively (detailed on the y-axis and in the titles) are plotted against iteration number for all three different activity concentrations studied for ^{89}Zr. Abbreviation: SB-JR, **S**ingle-**B**and **J**oint **R**econstruction; mMB-JR, **m**ixed **M**ulti-**B**and **J**oint **R**econstruction; MB-JR, **M**ulti-**B**and **J**oint **R**econstruction.

concentrations of 100 kBq ml^{-1} and 50 kBq ml^{-1} (figure A1). At these lower activity concentrations, image quality deteriorated, though JR methods still produced visually superior images. The primary cause of degradation was due to natural background (section 2.2.1), which becomes increasingly dominant at low activities—when excluded from simulations, all rod sectors became visible at both concentrations. This occurs because, with the clustered pinhole collimator employed in this study, photopeak counts from the Derenzo phantom become substantially smaller than the constant natural background contribution at these activity levels. Hence, we suggest that high sensitivity collimators and/or thicker detectors would be more suitable for achieving practical activity concentration levels with this isotope. This work focuses on developing a JR method, and optimizing the scanner hardware for a specific isotope lies outside the scope of this study.

Besides, to apply the proposed dual-photopeak JR methods in case of PET radionuclides with prompt emissions, we have modeled the positron range effect in the system matrix and applied JR to ^{89}Zr imaging. In the future, we would like to test these methods for other PET radionuclides, such as ^{124}I, ^{52}Mn. The relative intensities of annihilation photons and prompt gammas can vary substantially for different isotopes and benefits of JR may be dependent on these relative intensities. Note that in the proposed MB-JR and mMB-JR frameworks, these differences in emission yields were explicitly modeled through the factor τ_i (section 2.3.1), while in the SB-JR approach, yield variations are indirectly accounted for by incorporating the constituent gamma energies and intensities to compute a weighted average energy (equation (3)).

The use of more than two photopeaks in JR represents a promising direction for future research, as the inclusion of additional photopeaks—depending on the isotope—may further enhance image quality.

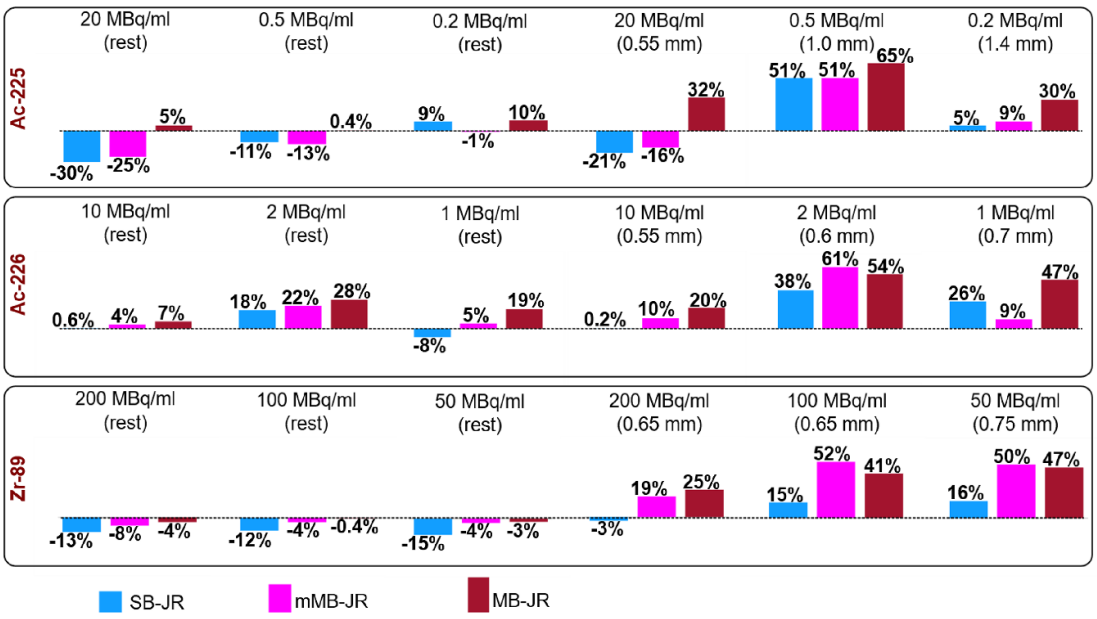

Figure 10. Percentage improvement (or degradation) of CNR of smallest visible sector and mean CNR (over rest of the visible sectors) at 60th (^{225}Ac, ^{226}Ac) and 100th (^{89}Zr) iterations due to three proposed joint reconstruction schemes over images from the best performing photopeak.

For each isotope, however, it is essential to evaluate which energy peaks are appropriate for incorporation into the JR. In this study, we provide a general methodology and illustrate its applicability through several representative examples.

The ^{89}Zr spectrum exhibits a substantial down scatter contribution to the 511 keV photopeak due to 909 keV prompt gammas (figure 3). In this study, the TEW scatter correction method (Goorden *et al* 2016) was employed. The TEW approach estimates the scatter component under the photopeak through linear interpolation between adjacent energy windows, which represents a simplification relative to the actual scatter distribution. Nonetheless, Beekman *et al* (2021) successfully applied the TEW method for experimental ^{89}Zr imaging, achieving high quantitative accuracy.

Our study demonstrated that the proposed methods—particularly the MB-JR approach—achieve improved imaging performance compared to reconstructions based on individual photopeaks in a multi-pinhole SPECT system. Although most clinical SPECT scanners employ parallel-hole collimators, we anticipate that similar benefits may be observed, especially in low-count scans, due to improved statistics. It is worth noting that the incorporation of both the 171 keV (91%) and 245 keV (94%) photopeaks of ^{111}In for imaging has been reported in certain clinical studies (Rowe *et al* 2015, Ravizzini *et al* 2023). However, in contrast to preclinical imaging, accurate attenuation correction for both photopeaks becomes essential in clinical applications.

Finally, we believe one of the major challenges in extracting larger improvements through JR methods across diverse modalities (Chun *et al* 2020, Roser *et al* 2022, Ghosh and Das 2023, Li *et al* 2024, Takyu *et al* 2025) was that, based on the scanner system design, different emissions have varying levels of quality (retrievable information from individual emission, on average) and sensitivity. Indeed various subsystems of a scanner are designed synergistically to extract out the best imaging performance from a specific or narrow band of emissions. A more bottom–up design approach (Lee *et al* 2020), which balances the levels of quality and sensitivity extracted from these different emissions, can enhance the performance of these software solutions. For example, in multi-pinhole SPECT, a hybrid collimator design incorporating pinholes with varying opening angles (Muslimov *et al* 2021), including some smaller than those optimal for 511 keV, improves the quality of 909 keV gamma detection through reduced edge penetration, and may enhance JR performance.

5. Conclusion

This study demonstrates that JR methods leveraging two photopeak emissions can enhance image quality of preclinical systems for both SPECT and PET radionuclides, especially in low-count scans.

Among the proposed approaches, the MB-JR scheme consistently yielded the best performance in almost all cases, albeit with increased computational demand. These methods may become promising for improved small and/or low-uptake lesion detectability in preclinical imaging but maybe also in clinical SPECT. Furthermore, the results indicate that their applicability can enable improved quantitative accuracy, which e.g. is important for diagnostics and image-based dosimetry protocols for therapeutic radionuclides.

Data availability statement

All data that support the findings of this study are included within the article (and any supplementary information files).

Acknowledgments

This work was supported by the research grant QUARAT: Quantitative Universal Radiotracer Tomography (TTW16885), which is partially funded by the Dutch Research Council (NWO).

Appendix

A.1. ^{225}Ac imaging

The total activity of ^{225}Ac that can be administered to a typical mouse without inducing radiotoxic effects ranges from 20 to 40 kBq/mouse (Nedrow *et al* 2017, Kelly *et al* 2020, Qin *et al* 2020, Meyer *et al* 2022, Ingham *et al* 2024). Recent advances using pre-targeted radioimmunotherapy (PRIT) methods have increased this limit to 296 kBq/mouse (Cheal *et al* 2020). Based on these total injected activity values and typical tumor uptake of 5%–40% (in %IA/ml) for this isotope (Nedrow *et al* 2017, Cheal *et al* 2020, Qin *et al* 2020, Banerjee *et al* 2021, Ingham *et al* 2024), we tried to guess a rough estimate of realistic activity concentration range to be 1–118 kBq ml^{-1} in typical mouse scan.

It is noteworthy that the lowest activity concentration reported in section 3.2 for this isotope is 200 kBq/mL, which lies just above the upper limit of the estimated realistic activity concentration range. To further evaluate the applicability of the proposed JR methods under realistic conditions, we conducted additional studies using a Derenzo resolution phantom (rod diameters 3.1–1.6 mm) filled with activity concentrations of 100 and 50 kBq/ml, both within the practical range. The corresponding reconstructed images, with and without natural background (NB, section 2.2.1) included in the projections, are provided in figure A1.

In the absence of NB, resolution of the reconstructed phantoms improved markedly. This observation is consistent with expectations, as for the cluster pinhole collimator employed in this study, the contribution of photopeak counts from the Derenzo phantom becomes relatively minor compared to NB at low activity concentrations. Specifically, at 100 kBq ml^{-1}, NB counts in the 218 keV and 440 keV photopeak windows were approximately 3.8 and 4.0 times higher than the phantom counts, respectively, while at 50 kBq ml^{-1} these ratios increased to 7.7 and 8.1.

A.2. Energy subsetting

We investigated the impact of different energy subsetting strategies within the MB-JR framework for all radionuclides and their respective activity levels (figure A2). In the first approach (MB-JR in figure A2), a total of 256 subsets were used, with the first 128 subsets corresponding to the lower energy gamma

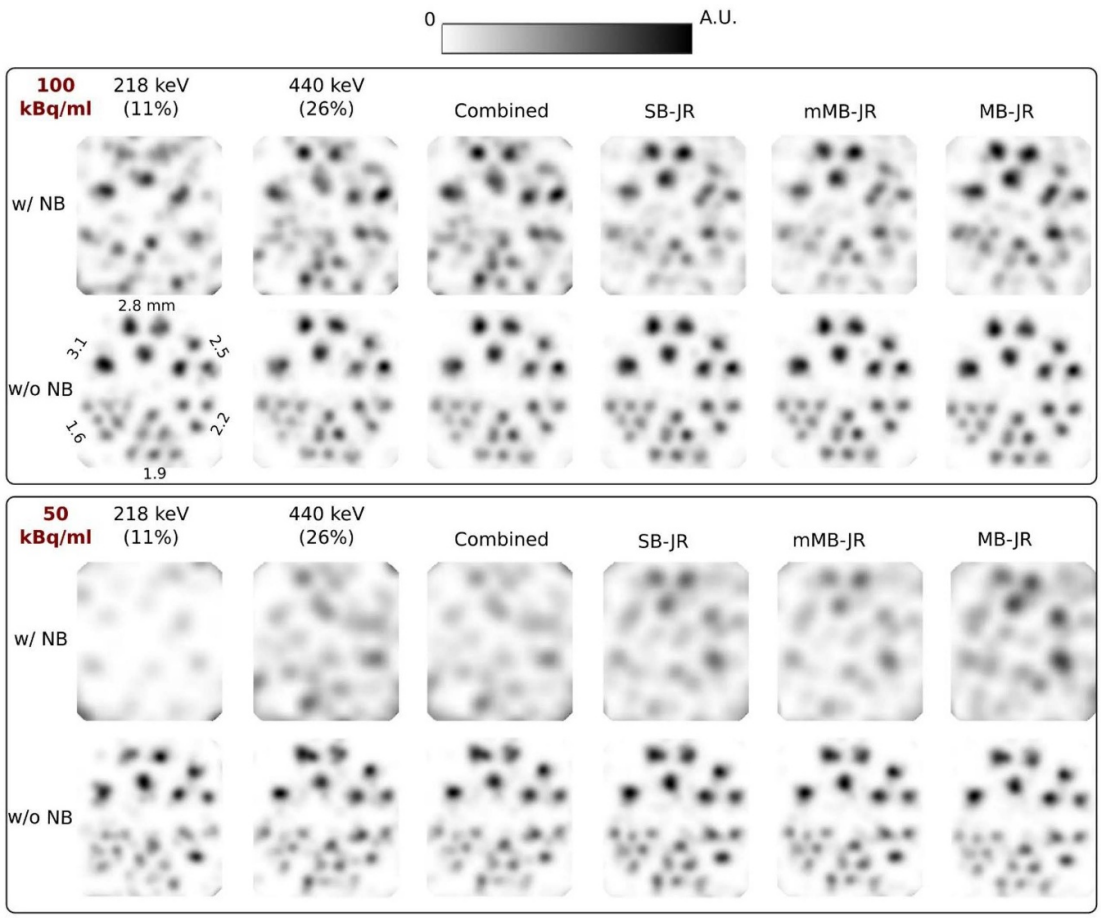

Figure A1. Derenzo resolution phantom images of ^{225}Ac after 30th iterations are shown for individual photopeaks (218 keV and 440 keV), two photopeak images combined after reconstruction, and three joint reconstruction schemes at two activity concentrations—100 and 50 kBq ml^{-1}. Post-filters FWHM 2.1/1.5 mm for w/ and w/o NB at 100 kBq ml^{-1}, 2.2/1.7 mm at 50 kBq ml^{-1}. Abbreviation: A.U., arbitrary unit; NB, natural background.

emissions and the remaining 128 subsets to the higher energy gamma emissions. In the alternative approach (MB-JR-mES), a total of 128 subsets were employed, each containing an equal mix from both the lower and higher energy gamma emissions. Visual inspection revealed that the reconstructed images produced by MB-JR and MB-JR-mES were largely similar across all radionuclides. Consequently, a CNR analysis, similar to section 3.3, was performed using three noise realizations. In nearly all cases, MB-JR demonstrated marginally superior performance compared to MB-JR-mES.

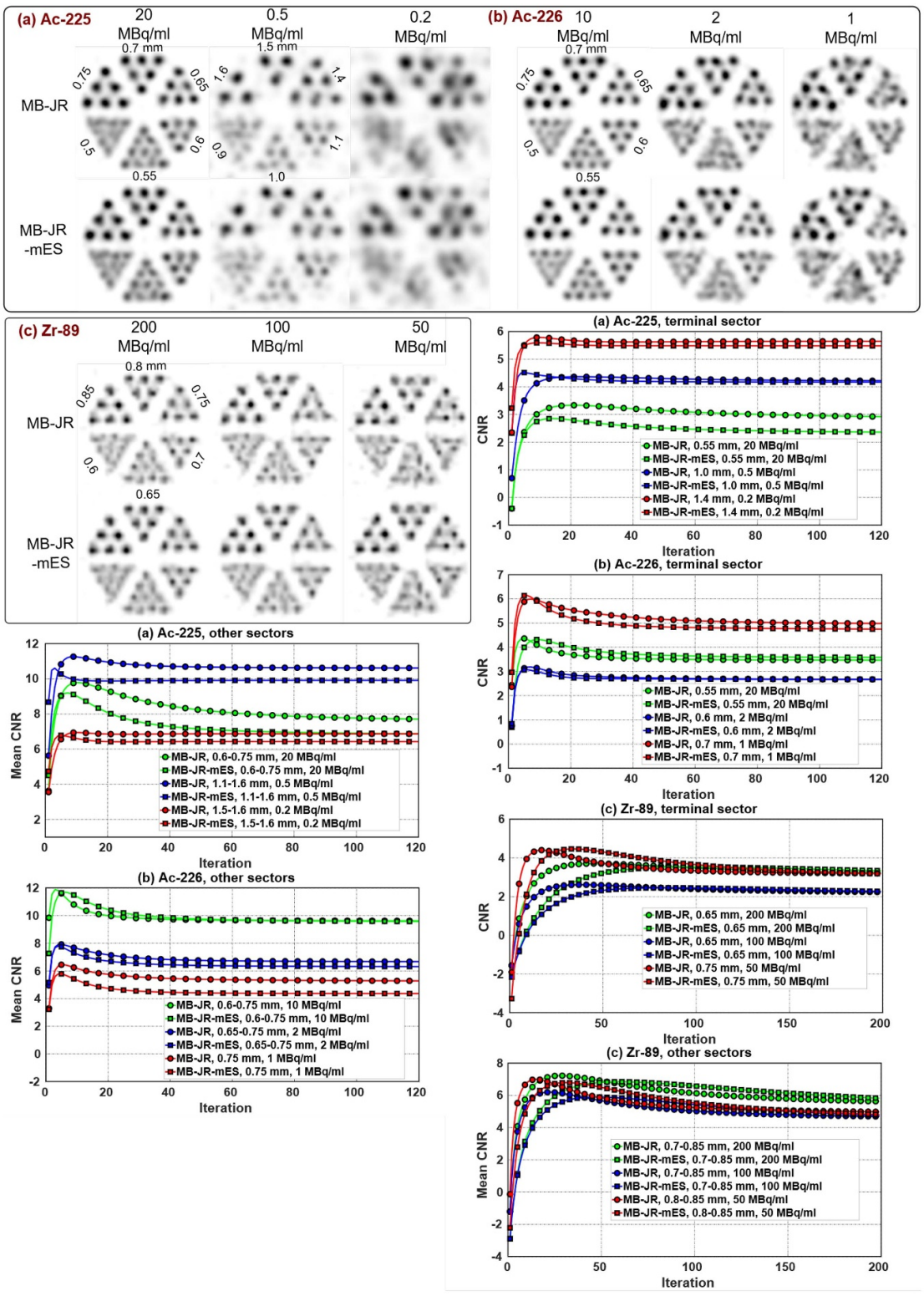

Figure A2. The 30th iteration resolution phantom images are shown for MB-JR and MB-JR-mES reconstruction for radionuclides—(a) ^{225}Ac, (b) ^{226}Ac, and similarly 100th iteration images for (c) ^{89}Zr—along with similar CNR analysis as in section 3.3.

ORCID iDs

Satyajit Ghosh 0000-0001-6334-1185
Valerio Cosmi 0009-0008-2748-2202
Marlies C Goorden 0009-0007-2202-5371

References

Agostinelli S *et al* 2003 Geant4-a simulation toolkit *Nucl. Instrum. Methods Phys. Res. A* **506** 250–303

Banerjee S R *et al* 2021 Preclinical evaluation of ^{213}Bi-and ^{225}Ac-labeled low-molecular-weight compounds for radiopharmaceutical therapy of prostate cancer *J. Nucl. Med.* **62** 980–8

Beekman F J 2011 Focused pinhole gamma detection device *US Patent* 8067741 B2

Beekman F J, Kamphuis C, Koustoulidou S, Ramakers R M and Goorden M C 2021 Positron range-free and multi-isotope tomography of positron emitters *Phys. Med. Biol.* **66** 065011

Bidkar A P, Zerefa L, Yadav S, VanBrocklin H F and Flavell R R 2024 Actinium-225 targeted alpha particle therapy for prostate cancer *Theranostics* **14** 2969–92

Borgna F, Haller S, Rodriguez J M, Ginj M, Grundler P V, Zeevaart J R, Köster U, Schibli R, van der Meulen N P and Müller C 2022 Combination of terbium-161 with somatostatin receptor antagonists—a potential paradigm shift for the treatment of neuroendocrine neoplasms *Eur. J. Nucl. Med. Mol. Imaging* **49** 1113–26

Branderhorst W, Vastenhouw B and Beekman F J 2010 Pixel-based subsets for rapid multi-pinhole SPECT reconstruction *Phys. Med. Biol.* **55** 2023

Cheal S M *et al* 2020 Alpha radioimmunotherapy using ^{225}Ac-proteus-DOTA for solid tumors—safety at curative doses *Theranostics* **10** 11359–75

Chun S Y, Nguyen M P, Phan T Q, Kim H, Fessler J A and Dewaraja Y K 2020 Algorithms and analyses for joint spectral image reconstruction in Y-90 bremsstrahlung SPECT *IEEE Trans. Med. Imaging* **39** 1369–79

Das B, Mehrdel B, Goodman D, Streicher M, Seo Y and Caravaca J 2025 Compton imaging of Ac-225 in pre-clinical phantoms with a 3D-positioning CZT camera *IEEE Trans. Radiat. Plasma Med. Sci.* 1

De Kruijff R M, Raavé R, Kip A, Molkenboer-Kuenen J, Morgenstern A, Bruchertseifer F, Heskamp S and Denkova A G 2019 The *in vivo* fate of ^{225}Ac daughter nuclides using polymersomes as a model carrier *Sci. Rep.* **9** 11671

De Kruijff R M, Wolterbeek H T and Denkova A G 2015 A critical review of alpha radionuclide therapy—how to deal with recoiling daughters? *Pharmaceuticals* **8** 321–36

de Swart J, Chan H S, Goorden M C, Morgenstern A, Bruchertseifer F, Beekman F J, de Jong M and Konijnenberg M W 2016 Utilizing high-energy γ-photons for high-resolution ^{213}Bi SPECT in mice *J. Nucl. Med.* **57** 486–92

Dekempeneer Y *et al* 2019 Labeling of Anti-HER2 nanobodies with astatine-211: optimization and the effect of different coupling reagents on their *in vivo* behavior *Mol. Pharm.* **16** 3524–33

Dey T, Backus B E, Romijn R L, Wieczorek H and Verzijlbergen J F 2014 Low-dose single acquisition rest ^{99m}Tc/stress ^{201}Tl myocardial perfusion SPECT protocol: phantom studies and clinical validation *Eur J. Nucl. Med. Mol. Imaging* **41** 536–47

Foxton C, Waldron B, Grønlund R V, Simón J J, Cornelissen B, O'Neill E and Stevens D 2025 Preclinical evaluation of 177Lu-rhPSMA-10.1, a radiopharmaceutical for prostate cancer: biodistribution and therapeutic efficacy *J. Nucl. Med.* **66** 599–604

Ghosh S, Cosmi V, Ramakers R M, Beekman F J and Goorden M C 2025 Ultra-high energy spectral prompt PET *Phys. Med. Biol.* **70** 075010

Ghosh S and Das P 2023 Single-cell tracking with compton-PET: an in silico feasibility study *Nucl. Instrum. Methods Phys. Res. A* **1053** 168373

Goorden M C, Kamphuis C, Ramakers R M and Beekman F J 2020 Accelerated image reconstruction by a combined dual-matrix dual-voxel approach *Phys. Med. Biol.* **65** 105014

Goorden M C, van der Have F, Kreuger R and Beekman F J 2011 An efficient simulator for pinhole imaging of PET isotopes *Phys. Med. Biol.* **56** 1617–34

Goorden M C, van der Have F, Kreuger R, Ramakers R M, Vastenhouw B, Burbach J P H, Booij J, Molthoff C F M and Beekman F J 2013 VECTor: a preclinical imaging system for simultaneous submillimeter SPECT and PET *J. Nucl. Med.* **54** 306–12

Goorden M C, van Roosmalen J, van der Have F and Beekman F J 2016 Optimizing modelling in iterative image reconstruction for preclinical pinhole PET *Phys. Med. Biol.* **61** 3712–33

Holzwarth U, Ojea Jimenez I and Calzolai L 2018 A random walk approach to estimate the confinement of α-particle emitters in nanoparticles for targeted radionuclide therapy *EJNMMI Radiopharm. Chem.* **3** 9

Ingham A *et al* 2024 Preclinical evaluation of [^{225}Ac]Ac-crown-TATE—An alpha-emitting radiopharmaceutical for neuroendocrine tumors *Nucl. Med. Biol.* **138** 108944

Jan S *et al* 2004 GATE: a simulation toolkit for PET and SPECT *Phys. Med. Biol.* **49** 4543

Jarvis P, Ho A and Sundram F 2021 Radium-223 therapy for metastatic castration-resistant prostate cancer: survival benefit when used earlier in the treatment pathway *Nucl. Med. Commun.* **42** 332–6

Jentzen W, Freudenberg L, Eising E G, Sonnenschein W, Knust J and Bockisch A 2008 Optimized ^{124}I PET dosimetry protocol for radioiodine therapy of differentiated thyroid cancer *J. Nucl. Med.* **49** 1017–23

Kelly V J, Wu S, Gottumukkala V, Coelho R, Palmer K, Nair S, Erick T, Puri R, Ilovich O and Mukherjee P 2020 Preclinical evaluation of an ^{111}In/^{225}Ac theranostic targeting transformed MUC1 for triple negative breast cancer *Theranostics* **10** 6946–58

Koniar H, McNeil S, Wharton L, Ingham A, Van de Voorde M, Ooms M, Sekar S, Rodríguez-Rodríguez C, Kunz P and Radchenko V 2024 Quantitative SPECT imaging of ^{155}Tb and ^{161}Tb for preclinical theranostic radiopharmaceutical development *EJNMMI Phys.* **11** 77

Koniar H, Rodríguez-Rodríguez C, Radchenko V, Yang H, Kunz P, Rahmim A, Uribe C and Schaffer P 2022 SPECT imaging of ^{226}Ac as a theranostic isotope for ^{225}Ac radiopharmaceutical development *Phys. Med. Biol.* **67** 185009

Lee H-J, Lee K-S and Cha H M 2020 Variable pinhole collimator and radiographic imaging device using same *US Patent* 10631795 B2

Li Z, Benabdallah N, Laforest R, Wahl R L, Thorek D L J and Jha A K 2024 Joint regional uptake quantification of thorium-227 and radium-223 using a multiple-energy-window projection-domain quantitative SPECT method *IEEE Trans. Med. Imaging* **43** 4281–93

Liu F-S, Wang S-Y, Shiau Y-C and Wu Y-W 2019 The clinical value and safety of ECG-gated dipyridamole myocardial perfusion imaging in patients with aortic stenosis *Sci. Rep.* **9** 12443

Majkowska-Pilip A, Gawęda W, Żelechowska-Matysiak K, Wawrowicz K and Bilewicz A 2020 Nanoparticles in targeted alpha therapy *Nanomaterials* **10** 1366

Mapanao A K *et al* 2025 Preclinical investigation of [^{149}Tb]Tb-DOTATATE and [^{149}Tb]Tb-DOTA-LM3 for tumor-targeted alpha therapy *Eur J. Nucl. Med. Mol. Imaging* **52** 1383–98

Meyer C *et al* 2022 Comparison of PSMA-TO-1 and PSMA-617 labeled with gallium-68, lutetium-177 and actinium-225 *EJNMMI Res.* **12** 65

Müller C, Vermeulen C, Köster U, Johnston K, Türler A, Schibli R and van der Meulen N P 2017 Alpha-PET with terbium-149: evidence and perspectives for radiotheragnostics *EJNMMI Radiopharm. Chem.* **1** 5

Muslimov A R, Antuganov D O, Tarakanchikova Y V, Zhukov M V, Nadporojskii M A, Zyuzin M V and Timin A S 2021 Calcium carbonate core–shell particles for incorporation of ^{225}Ac and their application in local α-radionuclide therapy *ACS Appl. Mater. Interfaces* **13** 25599–610

Nedrow J R, Josefsson A, Park S, Bäck T, Hobbs R F, Brayton C, Bruchertseifer F, Morgenstern A and Sgouros G 2017 Pharmacokinetics, microscale distribution, and dosimetry of alpha-emitter-labeled anti-PD-L1 antibodies in an immune competent transgenic breast cancer model *EJNMMI Res.* **7** 57

Nelson B J, Wilson J, Andersson J D and Wuest F 2023 Theranostic imaging surrogates for targeted alpha therapy: progress in production, purification, and applications *Pharmaceuticals* **16** 1622

Nguyen M P, Goorden M C and Beekman F J 2020 EXIRAD-HE: multi-pinhole high-resolution ex vivo imaging of high-energy isotopes *Phys. Med. Biol.* **65** 225029

Ogawa K, Harata Y, Ichihara T, Kubo A and Hashimoto S 1991 A practical method for position-dependent Compton-scatter correction in single photon emission CT *IEEE Trans. Med. Imaging* **10** 408–12

Pandya D N, Bhatt N B, Almaguel F, Rideout-Danner S, Gage H D, Sai K K and Wadas T J 2019 ^{89}Zr-chloride can be used for immuno-PET radiochemistry without loss of antigen reactivity in vivo *J. Nucl. Med.* **60** 696–701

Qin Y, Imobersteg S, Blanc A, Frank S, Schibli R, Béhé M P and Grzmil M 2020 Evaluation of actinium-225 labeled minigastrin analogue [^{225}Ac]Ac-DOTA-PP-F11N for targeted alpha particle therapy *Pharmaceutics* **12** 1088

Ravizzini G, Erwin W, De Palatis L, Martiniova L, Subbiah V, Paolillo V, Mitchell J, McCoy A P, Gonzalez J and Mawlawi O 2023 Dosimetry of a novel ^{111}Indium-labeled anti-P-cadherin monoclonal antibody (FF-21101) in non-human primates *Cancers* **15** 4532

Robertson A K, Ramogida C F, Rodríguez-Rodríguez C, Blinder S, Kunz P, Sossi V and Schaffer P 2017 Multi-isotope SPECT imaging of the ^{225}Ac decay chain: feasibility studies *Phys. Med. Biol.* **62** 4406–20

Roser J, Barrientos L, Bernabéu J, Borja-Lloret M, Muñoz E, Ros A, Viegas R and Llosá G 2022 Joint image reconstruction algorithm in Compton cameras *Phys. Med. Biol.* **67** 155009

Rowe S P, Vicente E, Anizan N, Wang H, Leal J P, Lodge M A, Frey E C and Wahl R L 2015 Repeatability of radiotracer uptake in normal abdominal organs with ^{111}In-pentetreotide quantitative SPECT/CT *J. Nucl. Med.* **56** 985–8

Strosberg J *et al* 2017 Phase 3 trial of ^{177}Lu-Dotatate for midgut neuroendocrine tumors *New Engl. J. Med.* **376** 125–35

Sukthankar P, Avila L A, Whitaker S K, Iwamoto T, Morgenstern A, Apostolidis C, Liu K, Hanzlik R P, Dadachova E and Tomich J M 2014 Branched amphiphilic peptide capsules: cellular uptake and retention of encapsulated solutes *Biochim. Biophys. Acta* **1838** 2296–305

Tagawa S T *et al* 2013 Phase II study of lutetium-177–labeled anti-prostate-specific membrane antigen monoclonal antibody J591 for metastatic castration-resistant prostate cancer *Clin. Cancer Res.* **19** 5182–91

Takyu S *et al* 2025 A whole gamma imaging prototype for higher quantitative imaging of ^{89}Zr-labeled antibodies in a tumor mouse model *Phys. Med. Biol.* **70** 025012

Tschan V J, Busslinger S D, Bernhardt P, Grundler P V, Zeevaart J R, Köster U, van der Meulen N P, Schibli R and Müller C 2023 Albumin-binding and conventional PSMA ligands in combination with ^{161}Tb: biodistribution, dosimetry, and preclinical therapy *J. Nucl. Med.* **64** 1625–31

Tuy H K 1983 An inversion formula for cone-beam reconstruction *SIAM J. Appl. Math.* **43** 546–52

Vaissier P E B, Beekman F J and Goorden M C 2016 Similarity-regulation of OS-EM for accelerated SPECT reconstruction *Phys. Med. Biol.* **61** 4300

Vaissier P E B, Goorden M C, Vastenhouw B, van der Have F, Ramakers R M and Beekman F J 2012 Fast spiral SPECT with stationary γ-cameras and focusing pinholes *J. Nucl. Med.* **53** 1292–9

van der Have F, Ivashchenko O, Goorden M C, Ramakers R M and Beekman F J 2016 High-resolution clustered pinhole ^{131}Iodine SPECT imaging in mice *Nucl. Med. Biol.* **43** 506–11

Van Der Have F, Vastenhouw B, Ramakers R M, Branderhorst W, Krah J O, Ji C, Staelens S G and Beekman F J 2009 U-SPECT-II: an ultra-high-resolution device for molecular small-animal imaging *J. Nucl. Med.* **50** 599–605

Vastenhouw B and Beekman F J PMID: 17332628 2007 Submillimeter total-body murine imaging with U-SPECT-I *J. Nucl. Med.* **48** 487–93

Villena J L, Tapias G, Lage E, Kreuger R and Beekman F J 2010 Evaluation of a 25-511 keV list mode readout system for a large field-of-view gamma camera *IEEE Nuclear Science Symp. & Medical Imaging Conf.* pp 2168–73

Wong J Y C, Raubitschek A, Yamauchi D, Williams L E, Wu A M, Yazaki P, Shively J E, Colcher D and Somlo G 2010 A pretherapy biodistribution and dosimetry study of indium-111-radiolabeled trastuzumab in patients with human epidermal growth factor receptor 2-overexpressing breast cancer *Cancer Biother. Radiopharm.* **25** 387–94